April 2014

The Transport of Ship Emissions in the Strait of Malacca Using a High-Resolution WRF Simulation and Low-Resolution Gdas Data Coupled with Hysplit

Tristan James Hall
Florida State University

FLORIDA STATE UNIVERSITY

COLLEGE OF ARTS & SCIENCES

THE TRANSPORT OF SHIP EMISSIONS IN THE STRAIT OF MALACCA USING A HIGH-RESOLUTION WRF SIMULATION AND LOW-RESOLUTION GDAS DATA COUPLED WITH HYSPLIT

By

TRISTAN JAMES HALL

A Thesis submitted to the
Department of Earth, Ocean and Atmospheric Sciences
in partial fulfillment of the
requirements for the degree of
Master of Science

Degree Awarded:
Summer Semester, 2014

Tristan James Hall defended this thesis on 24 April 2014.
The members of the supervisory committee were:

Henry E. Fuelberg
Professor Directing Thesis

Robert Hart
Committee Member

Vasu Misra
Committee Member

The Graduate School has verified and approved the above-named committee members, and certifies that the thesis has been approved in accordance with university requirements.

ACKNOWLEDGMENTS

First and foremost, I would like to thank the love of my life, Catherine Williams – without her, my life would be incomplete. Her endless support guided me through the completion of my thesis. Secondly, I would like to thank my family for their encouragement. Thirdly, I would like to thank Dr. Henry E. Fuelberg for being my advisor and mentor. He has taught me how to be a better scientist.

I would like to thank the following people who helped in the completion of this work:

My committee members, Drs. Hart and Misra. They provided helpful insight to make this work more credible.

Present Fuelberg Lab members, Max, Dan, Nick, Daniel, Ari, Andy, Sean, and Ryan, and past members, Brannon and Antonio.

My friends within the EOAS and Musicology departments.

NASA grant NNX12AC07G (aka SEAC^{4}RS).

TABLE OF CONTENTS

List of Tables . . . vi

List of Figures . . . vii

Abstract . . . ix

1 Introduction **1**
- 1.1 Emissions from ships . . . 1
  - 1.1.1 Emission composition and impacts to environment . . . 1
  - 1.1.2 Emissions in the Strait of Malacca . . . 3
- 1.2 Convection near the Strait of Malacca . . . 5
  - 1.2.1 Diurnal variability of convection . . . 7
    - 1.2.1.1 Description of mesoscale circulations. . . . 8
  - 1.2.2 Seasonal variability . . . 12
- 1.3 Transport of ship emissions . . . 15
  - 1.3.1 Transport using global models . . . 17
  - 1.3.2 Transport using regional models . . . 19
- 1.4 Objectives . . . 20

2 Data and Methods **21**
- 2.1 Study periods . . . 21
- 2.2 WWLLN data . . . 21
- 2.3 HYSPLIT . . . 22
  - 2.3.1 Model specifics . . . 22
  - 2.3.2 Particle release specifics . . . 23
- 2.4 GDAS meteorological data . . . 23
- 2.5 The WRF Model . . . 24
  - 2.5.1 Verification of the WRF Model simulations . . . 26
- 2.6 EDGAR emissions data . . . 27

3 Results **32**
- 3.1 Winds . . . 32
  - 3.1.1 Low-level winds . . . 32
  - 3.1.2 Mid-level winds . . . 33
  - 3.1.3 Upper-level winds . . . 35
  - 3.1.4 Vertical wind profiles . . . 37
- 3.2 Trajectory analysis . . . 40
  - 3.2.1 April . . . 40
  - 3.2.2 October . . . 42
  - 3.2.3 February . . . 45
- 3.3 Vertical concentration and fluxes . . . 49

4 Summary and Conclusions **56**

References 62

Biographical Sketch 74

LIST OF TABLES

1 WRF Version 3.5 model parameters. 26

2 Summary of HYSPLIT particle locations after 120 h (CO proxy concentrations; pptv) summed over three layers within the entire domain for WRF [GDAS] for each of the three months of study. 58

LIST OF FIGURES

1 The Strait of Malacca region in Southeast Asia. The Strait of Malacca lies between the Malay Peninsula and the Indonesian island of Sumatra. 2

2 GOME-2 tropospheric column NO_2 [$\times 10^{13}$ molec. cm^{-2}] for a) February, b) April, and c) October 2011. Values over land are masked out to emphasize the contribution just from shipping. 5

3 WWLLN lightning strokes for January through December of 2005–2011. Counts for the entire 24 h period are shown. The stroke data were binned on a 0.25° × 0.25° grid encompassing the region. This grid resolution is reflective of the WWLLN location accuracy in the region (Section 2.2). 8

4 Lightning characteristics near the Strait during January–December 2005–2011. Results for three geographic regions are displayed. Colored bars and lines indicate stroke counts for the three regions (left axis). Solid lines indicate daytime (0700–1900 LT) strokes, and dashed lines indicate nighttime (1900–0700 LT) strokes. Pink bars indicate average thunderstorm days per month (right axis) for Kuala Lumpur International Airport, Malaysia (WMKK). “Sumatra” is defined as the northern tip of the island of Sumatra to the line that extends west from the southern tip of Singapore, and everything in between the two coasts. “Malaysia” is defined as the southern tip of Singapore to the line that extends east from the northern tip of the island of Sumatra, and everything in between the two coasts. “The Strait” is the body of water between the east coast of Sumatra and the west coast of the Malay Peninsula, and everything south of the line that defined the northern border of “Malaysia” and north of the line that defined the southern border of “Sumatra”. 9

5 WWLLN lightning climatology [strokes h^{-1}] for a) onshore (1100–2100 LT) and b) offshore (2100–1100 LT) maxima. The data are shown on a 0.25° × 0.25° grid. 11

6 GDAS analyses of 10 m winds [m s^{-1}] during a) February, b) April, c) October, and d) July. July is shown as a comparison of winds during the monsoon season. 14

7 Average (2005–2011) CAPE [J kg^{-1}] from the GDAS model for grid points within the Strait of Malacca. 15

8 Comparison of terrain height [m] between the a) GDAS and b) WRF models. 18

9 WRF computational domain. The outer domain (d01) has a horizontal grid spacing of 18 km. Domain 2 (d02) has a horizontal grid spacing of 6 km, and Domain 3 (d03) has a 2 km grid spacing. 25

10 The WRF model simulation characteristics of deep convection development and propagation in the Strait region. Winds [m s^{-1}] are shown at an interval of 14 km (7 grid cells). The color scale represents simulated maximum reflectivity [dBZ], and black contours represent WWLLN lightning observations. Red arrows represent sea breeze propagation, green arrows represent land breeze propagation, and blue arrows represent outflow boundaries associated with the convection. 28

11 Average 10 m winds from WRF (left) and GDAS (right) data during the three study periods (0000 UTC 14th day through 0000 UTC 21st day) of (a and b) April, (c and d) October, and (e and f) February 2011. Streamlines are thinned for the WRF-derived winds to better display the data. 34

12 As in Fig. 11, but for mid-level winds. 36

13 As in Figs. 11 and 12, but for upper-level winds. 38

14 Vertical motion profiles for WRF (solid) and GDAS (dashed) at grid points having at least 15 mm h^{-1} precipitation rate. Thresholds were selected based on grid-scale (convective parameterization) precipitation within WRF (GDAS). Vertical grid spacing is 1 km. 39

15 April WRF (left column) and GDAS (right column) HYSPLIT results. Concentrations of proxy CO particles are shown in pptv on a 0.25° × 0.25° × 1 km grid. Horizontal plots (a) and (b) are columnar sums from the surface to the model top, latitudinal cross sections (c and d) are domain sums that include all longitudes, and the longitudinal cross sections (e and f) include all latitudes. The black line below the plots between 1° and 6° N in (c) and (d) and 95° and 102° E in (e) and (f) is the approximate location of the Strait. 43

16 As in Fig. 15, but for October. 46

17 As in Figs. 15 and 16, but for February. 50

18 Vertical profiles of concentrations of HYSPLIT trajectories as a proxy for CO (pptv) at various levels from WRF (solid) and GDAS (dashed). Vertical grid spacing is 1 km. 52

19 CO mass flux for each study period calculated a) over the entire domain and b) only within the Strait. Sums within 1 km layers (solid) and net values (dashed). 55

ABSTRACT

The goal of this research is to describe and quantify the role of deep convection within the Strait of Malacca (hereafter referred to as the "Strait"; a part of the Maritime Continent in Southeast Asia) on the long-range transport of ship emissions. It utilizes a combination of the Weather Research and Forecasting (WRF) Model with a 2 km horizontal grid spacing and the HYbrid Single Particle Lagrangian Integrated Trajectories model (HYSPLIT_4). Results from the high-resolution WRF simulations are compared to the coarse-resolution (1° horizontal grid spacing) Global Data Assimilation System (GDAS) data provided by the Air Resources Laboratory. World Wide Lightning Network (WWLLN) observations reveal that the Strait region has a pronounced diurnal cycle of lightning with a nighttime (1900–0700 LT) maximum that is 2–3 times greater in the Strait itself than the daytime (0700–1900 LT) maximum on the surrounding landmasses. WWLLN observations also reveal that the Strait region has a seasonal cycle that is influenced by the Intertropical Convergence Zone and is out of phase with the Asian monsoon. April is the month with the most lightning, followed by October. Conversely, February is the month with the least amount of lightning. Therefore, these three months are the focus of this study. The Emissions Database for Global Atmospheric Research v4.2 is used to find an average emissions rate from ships within the Strait. A mass is assigned to each HYSPLIT particle in order to display a three-dimensional representation of CO concentrations.

HYSPLIT results using WRF as the meteorological input reveal that more CO is transported to the upper troposphere/lower stratosphere (UTLS) during April than any other month. October is also efficient at transporting CO to the UTLS, but in smaller concentrations than April. CO transport during February is primarily in the lower to middle troposphere. The effect of model resolution is shown by comparing WRF-derived trajectories to GDAS-derived trajectories. The coarse-resolution GDAS-derived trajectories remain close to their point of release after 120 h. The high-resolution WRF-derived trajectories exhibit more horizontal and vertical transport than GDAS. Result of vertical mass flux calculations

show that April has the greatest influence on the UTLS which is consistent with WWLLN lightning observations and a climatology of GDAS convective available potential energy within the Strait. April has the greatest hydrostatic instability of the three months studied, and therefore has the most lightning and deepest transport; October is second in this regard; and February is third.

CHAPTER 1

INTRODUCTION

The Strait of Malacca (Fig. 1), hereafter referred to as the "Strait," is the primary shipping lane connecting the Pacific and Indian Oceans, and by extension, the Arabian Sea, Persian Gulf, and Red Sea. The Strait lies between the Malay Peninsula and the Indonesian island of Sumatra, each containing a spine of mountains. On Sumatra, the Barisan Mountains peak above 3 km, while on Peninsular Malaysia, the Titiwangsa Mountains are ~2 km in height. The Strait itself is ~300 km wide at its northern extent and ~70 km at its southern limit.

The Strait ranks first in crude oil trade and third in dry bulk cargo trade in Asia (Streets et al. 1997; Dalsøren et al. 2009). It sees over 300 cargo vessels and tankers each day carrying 40% annually of all global oil trade (80% of the oil for Japan; Lepawsky 2005). Major shipping ports in and around the Strait (Fig. 1) include Singapore, Port Klang, Malaysia, and Tanjung Pelepas, Malaysia. Singapore was the second busiest port in the world in containers and tonnage in 2011, ranking only behind Shanghai, China (AAPA cited 2013; Salisbury cited 2013). Singapore and Malaysia both consistently ranked in the top 25 in the world during the past 4 years in the number of flags registered (U.S. DOT cited 2013).

1.1 Emissions from ships

1.1.1 Emission composition and impacts to environment

Ships are the world's greatest anthropogenic polluters in terms of per ton of fuel consumed (Corbett et al. 1999; Corbett and Koehler 2003). The emissions primarily consist of carbon dioxide (CO_2), nitrogen oxides (NO_x), sulfur dioxides (SO_x), carbon monoxide

FIG. 1. The Strait of Malacca region in Southeast Asia. The Strait of Malacca lies between the Malay Peninsula and the Indonesian island of Sumatra.

(CO), particulate matter (PM), volatile organic compounds (VOCs), and various secondary byproducts such as ozone (Endresen et al. 2003; Richter et al. 2004; Haglind 2008; Williams et al. 2009; Matthias et al. 2010). An estimated 11–15, 4–9, and 2–3% of all global anthropogenic emissions of NO_x, SO_2, and CO_2, respectively, came from ships during 2000 (Endresen et al. 2003; Eyring et al. 2010). Corbett et al. (1999) stated that ship emissions account for 14% of nitrogen and 2% of CO_2 emissions from fossil fuels, and 16% of all sulfur from petroleum uses. Shipping emits approximately 9.2 (80) and 0.8 (2.7) times more NO_x (SO_x) than aviation and road traffic, respectively (Eyring et al. 2005). On a regional basis, Asia ranks first with 46% of all SO_2 emissions from ships (Endresen et al. 2005).

Ship emissions are detrimental to the environment. Sulfate and nitrate deposition greatly affect coastal areas, typically producing a 3–10% increase in acidification, but as much as 50% in high occupancy regions (Endresen et al. 2003; Dalsøren et al. 2009). Deposition from nitrate and sulfate can modify environments by either increasing foreign plant growth or hindering the growth of local plants (Eyring et al. 2010). Although emissions of CO, NO_x, and VOCs can enhance surface ozone and methane oxidation that lead to greenhouse warming, no ship emission allocations were made to countries in the Kyoto Protocol (Endresen et al. 2003; Eyring et al. 2010). Conversely, Lawrence and Crutzen (1999) and Eyring et al. (2010) found that ships could contribute to global cooling due to the aerosols emitted and their subsequent modification of clouds.

1.1.2 Emissions in the Strait of Malacca

Since the Strait of Malacca contains a large amount of ship traffic, it is no surprise that the emissions from it are a significant source of local pollution. However, few papers have specifically addressed the large emission sources from ships in the confined Strait. A local maximum of Ship Emissions Allocation Factors was found within the Strait (Eyring et al. 2010). Beirle et al. (2004) showed that in the east-west shipping lane between Sri Lanka and Sumatra, NO_x emissions from ships approached background values at an approximate distance of 180–244 km away from the shipping lane. A majority of the width of the Strait is well within these bounds. The combination of major ship traffic in a narrow corridor makes the Strait a prime region for locally concentrated ship emissions.

Ships contributed one-quarter of the total SO_2 emissions and 4–12% of total sulfur deposition in Singapore, Peninsular Malaysia, and Sumatra, despite the presence of major local industrial sources (Streets et al. 1997). This study also found that ports alone accounted for 10% of the total sulfur emissions from ships. Near ports and heavily traveled waterways, such as the Strait, as much as 20% of SO_2 atmospheric loading came from ships (Streets et al. 2000; Dalsøren et al. 2009). Overall, Streets et al. (1997) found that 11.7% of all sulfur emissions in Southeast Asia came from ship emissions, with the lands most impacted being those bordering the Strait.

Satellite sensors can detect the atmospheric NO_x associated with shipping in the Strait (Beirle et al. 2004; Richter et al. 2004; and Franke et al. 2009), using instruments such as GOME (Global Ozone Monitoring Experiment; Burrows et al. 1999), GOME-2 (Callies et al. 2000), and SCIAMACHY (SCanning Imaging Absorption spectroMeter for Atmospheric CHartographY; Burrows et al. 1995; Bovensmann et al. 1999). Although these studies primarily focused on a shipping lane between Sri Lanka and Sumatra, a relative maximum also was observed within the Strait. An even better defined maximum is seen near Singapore (Fig. 2 in Richter et al. 2004; and Fig. 1 in Franke et al. 2009), but with a slight displacement to the east (Richter et al. 2004). The maximum near Singapore is consistent with Dalsøren et al. (2009). Figure 2 shows GOME-2 tropospheric column NO_2 for February, April, and October 2011. Although the total NO_2 signal in this figure cannot be attributed solely to ship emissions, the patterns within the Strait and the area between

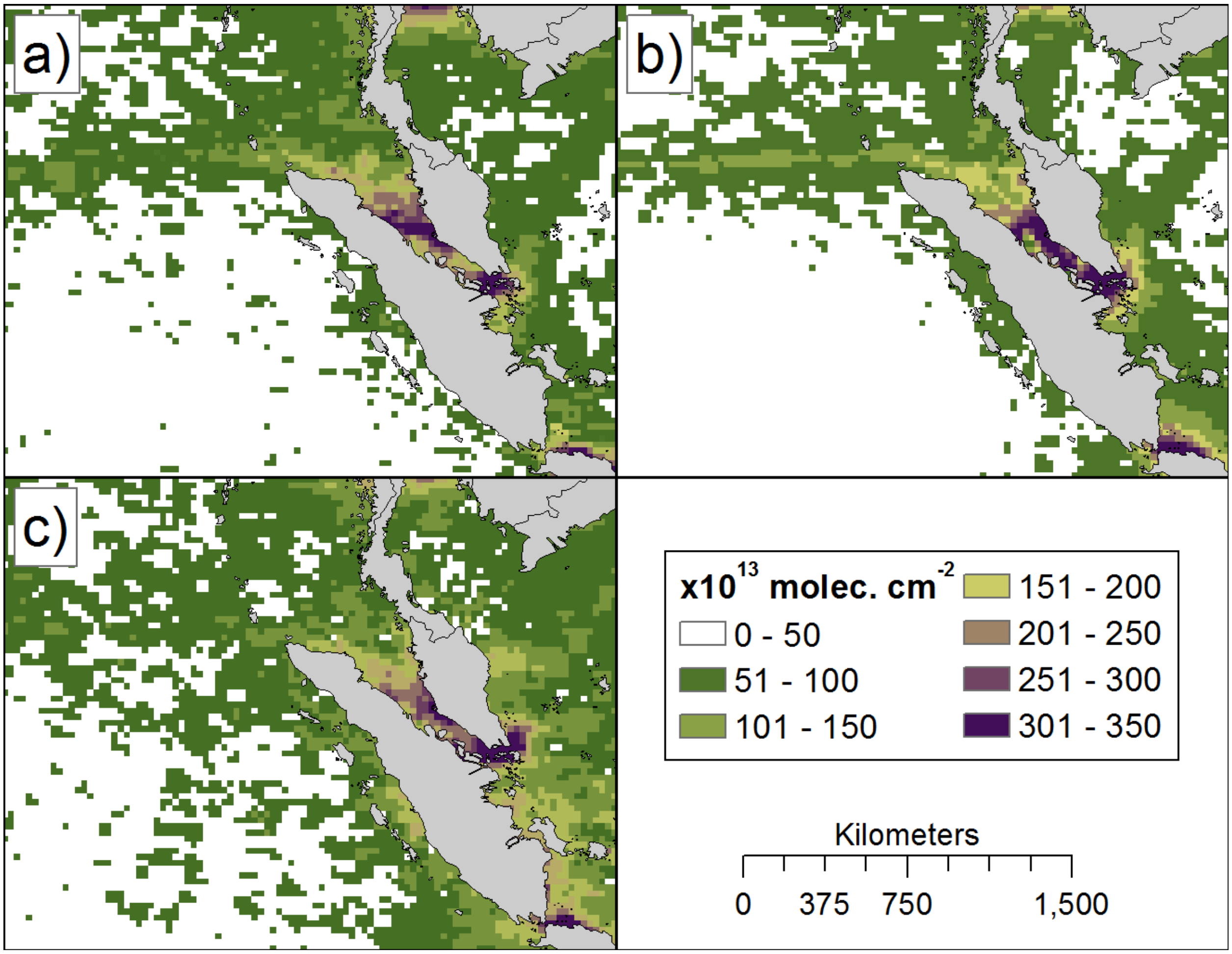

FIG. 2. GOME-2 tropospheric column NO_2 [$\times 10^{13}$ molec. cm^{-2}] for a) February, b) April, and c) October 2011. Values over land are masked out to emphasize the contribution just from shipping.

Sumatra and Sri Lanka (outside the figure) are consistent with those shown in Beirle et al. (2004), Richter et al. (2004), and Franke et al. (2009).

1.2 Convection near the Strait of Malacca

Deep convection can rapidly loft surface-based pollution into the upper troposphere where winds are stronger than near the surface (e.g., Klich and Fuelberg 2013; Heath and Fuelberg 2013, and references therein). The Maritime Continent of Southeast Asia, including the heavily polluted Strait of Malacca, is a region of widespread deep convection having a pronounced diurnal cycle (e.g., Ohsawa et al. 2001; Neale and Slingo 2003; Mori et al. 2004; Sakurai et al. 2005; Qian 2008; Fujita et al. 2010; Virts et al. 2013). Because of the Strait's geographical location, the seasonality of the convection is modulated by 1) monsoonal winds (e.g., Krishnamurti and Bhalme 1976; Meehl 1987; Hendon and Woodberry 1993; Ju and Slingo 1995; Yang and Slingo 2001; Loschnigg et al. 2003; Neale and Slingo 2003; Chang et al. 2005) and 2) the passage of the intertropical convergence zone (ITCZ; Crowe 1951; Beirle et al. 2004; Chang et al. 2005; Sakurai et al. 2005; Berry and Reeder 2013). Modulating the seasonal and intraseasonal variations in convection are 1) the Indian Ocean Dipole (e.g., Saji et al. 1999; Loschnigg et al. 2003), 2) El Niño (and its variations; e.g., Meehl 1987; Ju and Slingo 1995; Hamada et al. 2002; Chang et al. 2004; Aldrian et al. 2007), 3) the Madden-Julian oscillation (MJO; e.g., Wu and Hsu 2009; Virts et al. 2011; Rauniyar and Walsh 2011), 4) the tropospheric biennial oscillation (TBO; e.g., Meehl 1997), and 5) the quasi-biennial oscillation (QBO; e.g., Lindzen and Holton 1968). The deep convection over the Maritime Continent contributes to the Hadley and Walker circulations (Ramage 1968; Houze et al. 1981; Neale and Slingo 2003), as well as secondary circulations described by Krishnamurti (1971) and Krishnamurti et al. (1973).

The current research period is too short to isolate and quantify the contributions of the Hadley and Walker circulations or consider the contributions from intraseasonal variations such as the TBO, MJO, QBO, Indian Ocean Dipole, and El Niño. Instead, the focus is on prominent mesoscale circulations that determine the exact timing and location of the widespread, almost daily convection, and how the convection, once formed, influences atmospheric transport. Prominent mesoscale circulations include the sea/land breeze and katabatic/anabatic winds that are due to the complex field of islands, warm sea surface temperatures, and mountains in the region.

1.2.1 Diurnal variability of convection

The study region has a pronounced climatological lightning maximum that is indicative of extensive deep convection. Due to the juxtaposition of land, mountains, and water, there is also a distinct diurnal pattern of convection over the Strait and its surrounding landmasses. The lightning maximum has been shown independently by the Lightning Imaging Sensor (Christian et al. 1999) aboard NASA's Tropical Rainfall Measuring Mission satellite (e.g., Boccippio et al. 2000; Petersen and Rutledge 2001), the Optical Transient Detector (Christian et al. 1996) aboard the MicroLab-1 satellite (e.g., Boccippio et al. 2000; Christian et al. 2003), and the World Wide Lightning Location Network (WWLLN, see http://wwlln.net; and Virts et al. 2011, 2013). Figure 3 displays this maximum in terms of the average number of lightning strokes per year based on 7 years of data (2005–2011) from the WWLLN (described in the next chapter).

To quantify the WWLLN-derived lightning strokes in the study region, Fig. 4 contains stroke counts for three different sub-areas: Sumatra, the Strait, and the Malay Peninsula. The number of thunderstorm days reported at the nearby Kuala Lumpur International Airport, Malaysia (WMKK) is also displayed (data from wunderground.com). The large total stroke count over the Strait is immediately apparent, as are maxima during April and October (the seasonal nature of this figure is discussed later). Nighttime strokes within the Strait (0700–1900 LT; LT=UTC+7) outnumber daytime strokes (1900–0700 LT)—opposite that of the landmasses, where daytime strokes are more numerous than nighttime.

The nighttime climatological maximum over the Strait (Fig. 4) and the maximum within the Strait (Fig. 3) are attributed to the combined effects of sea/land breezes, mountain/valley breezes, and the convergence of cold-air outflow from storms originating over the mountains of Sumatra and the Malay Peninsula (Ramage 1964; Oki and Musiake 1994; Ohsawa et al. 2001; Sakurai et al. 2005; Fujita et al. 2010). Gray and Jacobson (1977) found

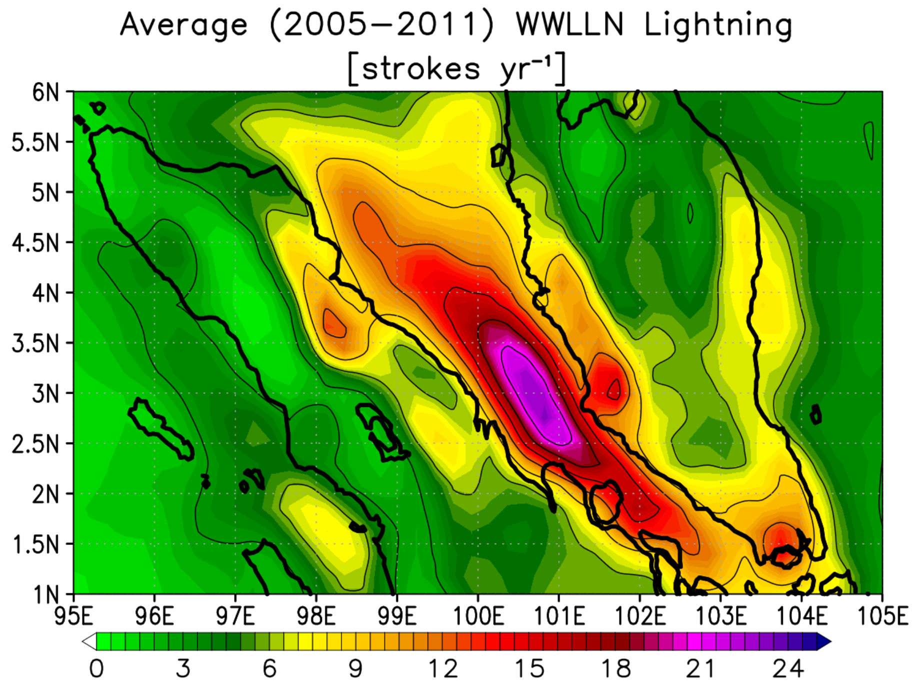

Fig. 3. WWLLN lightning strokes for January through December of 2005–2011. Counts for the entire 24 h period are shown. The stroke data were binned on a 0.25° × 0.25° grid encompassing the region. This grid resolution is reflective of the WWLLN location accuracy in the region (Section 2.2).

that heavy rainfall in the tropics during the early morning (0300–0600 LT) is 2–3 times greater than in the late afternoon-evening (1800–0000 LT). The stroke counts in Fig. 4 are consistent with these results, where the daytime (0700–1900 LT) counts are 2–3 times greater than nighttime (1900–0700 LT) counts over land, and vice versa over the Strait. Maximum precipitation throughout the Strait occurs between the hours of 0000 and 0800 LT (Ohsawa et al. 2001).

1.2.1.1 Description of mesoscale circulations. A convenient starting point for describing the primary mesoscale mechanisms producing deep convection near the Strait is the initiation of the sea breeze during the day on either or both surrounding landmasses. When the thermal contrast between warmer land and cooler water becomes sufficiently great,

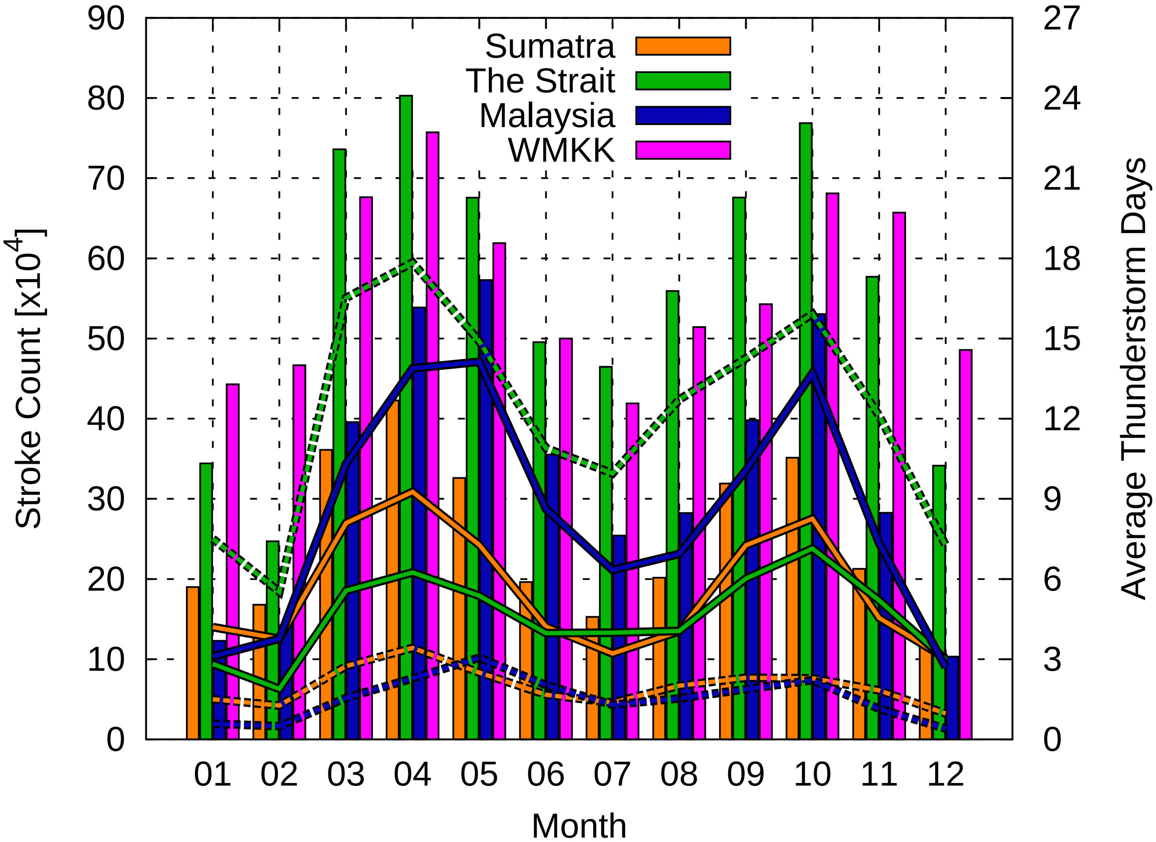

FIG. 4. Lightning characteristics near the Strait during January–December 2005–2011. Results for three geographic regions are displayed. Colored bars and lines indicate stroke counts for the three regions (left axis). Solid lines indicate daytime (0700–1900 LT) strokes, and dashed lines indicate nighttime (1900–0700 LT) strokes. Pink bars indicate average thunderstorm days per month (right axis) for Kuala Lumpur International Airport, Malaysia (WMKK). "Sumatra" is defined as the northern tip of the island of Sumatra to the line that extends west from the southern tip of Singapore, and everything in between the two coasts. "Malaysia" is defined as the southern tip of Singapore to the line that extends east from the northern tip of the island of Sumatra, and everything in between the two coasts. "The Strait" is the body of water between the east coast of Sumatra and the west coast of the Malay Peninsula, and everything south of the line that defined the northern border of "Malaysia" and north of the line that defined the southern border of "Sumatra".

the sea breeze initiates. It consists of on-shore, low-level flow that penetrates farther inland as the temperature contrast increases during the day. The sea breeze in the region of the Strait begins around 1000–1100 LT on either or both coasts of the surrounding landmasses regardless of season (e.g., Ramage 1964; Mori et al. 2004; Sakurai et al. 2005; Joseph et al. 2008; Qian 2008; Hara et al. 2009; Fujita et al. 2010; Love et al. 2011).

The sea breeze circulations are influenced by the large scale winds and aided by up-slope, anabatic flow (e.g., Kimura and Kuwagata 1995; Ohsawa et al. 2001; Yang and Slingo 2001; Wu et al. 2003; Rampanelli et al. 2004; Sasaki et al. 2004; Joseph et al. 2008; Qian 2008; Fujita et al. 2010). During periods of light synoptic-scale winds, these circulations form on both sides of the two landmasses and can propagate inland to converge over the Barisan and Titiwangsa Mountains near the centers of the two landmasses (Mori et al. 2004; Joseph et al. 2008; Qian 2008; Fujita et al. 2010; Love et al. 2011). The low-level convergence leads to maximum onshore precipitation during the late afternoon-early evening (1800–2000 LT) hours (Ohsawa et al. 2001; Yang and Slingo 2001; Mori et al. 2004; Sakurai et al. 2005; Joseph et al. 2008; Hara et al. 2009; Fujita et al. 2010). Figure 5 shows the horizontal distribution of WWLLN observations during the times of maximum onshore (a; 1100–2100 LT) and offshore (b; 2100–1100 LT) convection. During the time of maximum convection over land, there typically is little or no convection over the Strait due to the return flow and subsidence in the mid-to-lower troposphere. Arritt (1989) found that the offshore extent of the onshore sea breeze is approximately 100 km—a characteristic seen in satellite imagery off the coast of Florida (Pett and Tag 1984).

The early-evening peak in precipitation over the mountains of either landmass (Fig. 5a) initiates outflow boundaries that propagate downward toward the coast (Mori et al. 2004; Sakurai et al. 2005; Fujita et al. 2010; Love et al. 2011). These boundaries can be in the form of coupled rainfall-generated, cold-air outflow (a type of gravity wave), down-slope

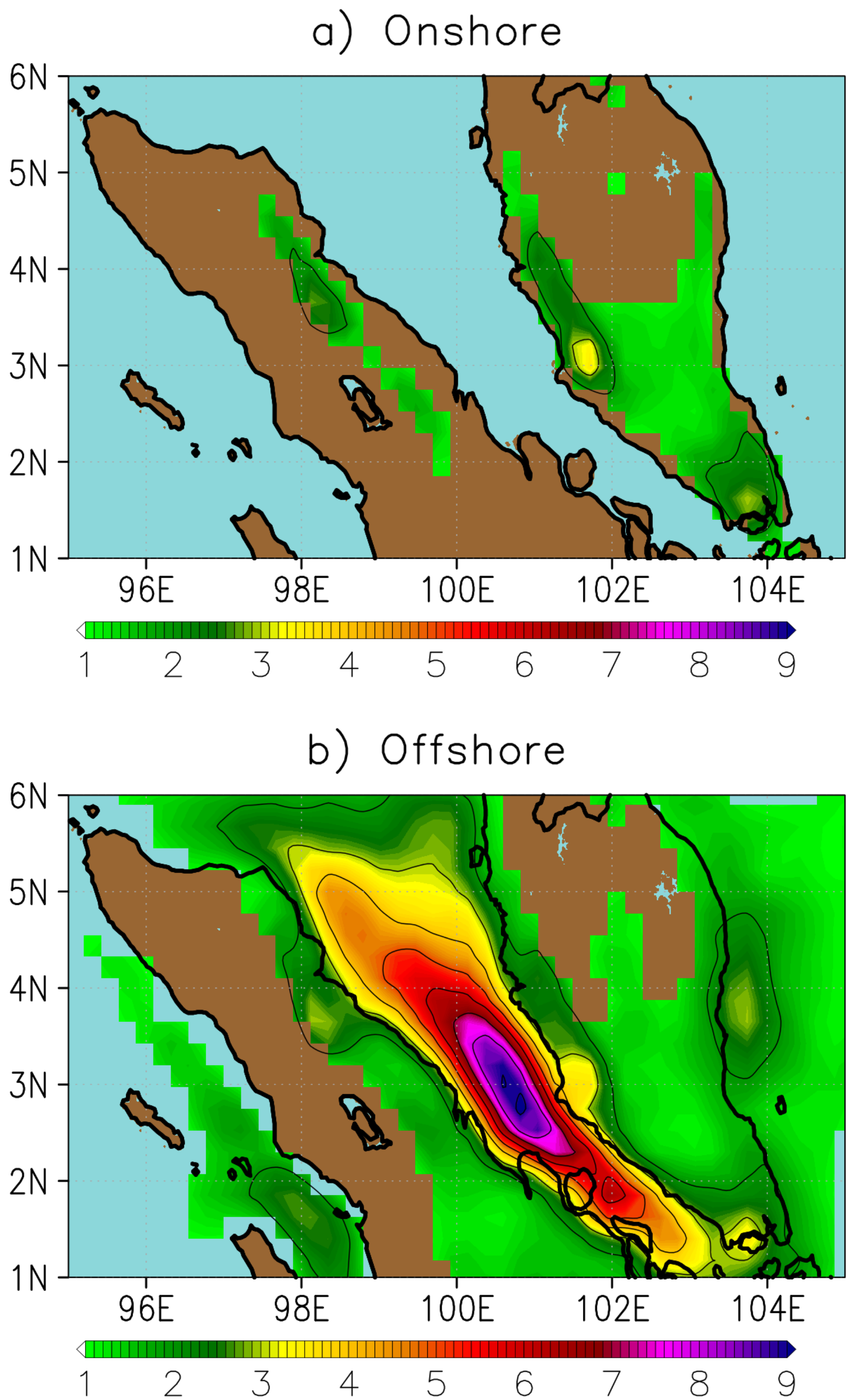

FIG. 5. WWLLN lightning climatology [strokes h^{-1}] for a) onshore (1100–2100 LT) and b) offshore (2100–1100 LT) maxima. The data are shown on a $0.25° \times 0.25°$ grid.

katabatic wind complexes (e.g., Feng and Chen 1998; Fujita et al. 2010; Love et al. 2011), or a propagating mesoscale convective system (Nesbitt and Zipser 2003; Sakurai et al. 2005; Hara et al. 2009). The offshore moving land breeze that develops after sunset (Qian 2008; Fujita et al. 2010) further enhances this combination of flows. Houze et al. (1981) found similar results when studying deep convection near North Borneo.

By morning (0300–0900 LT), the combined land breeze, gravity wave, or cold-air outflow have propagated over the Strait from Sumatra and the Malay Peninsula. Large-scale winds can influence the propagation, but the flows often collide over the Strait (Ramage 1964; Ohsawa et al. 2001; Mori et al. 2004; Hara et al. 2009; Fujita et al. 2010; Love et al. 2011). Ramage (1964) showed that converging land breezes are more common over the narrow southern regions of the Strait than the wider northern portions. The morning convergence leads to maximum convection over the Strait (Fig. 5b).

To summarize, the local terrain and subsequent land/sea breezes, mountain/valley circulations, and outflow boundaries greatly modulate the diurnal cycle of deep convection near the Strait. The Strait itself experiences more nighttime (1900–0700 LT) lightning than either surrounding landmass during the daytime (0700–1900 LT). Conversely, the landmasses have more lightning during the daytime than the nighttime (Figs. 4 and 5).

1.2.2 Seasonal variability

The seasonal movement of the ITCZ and changing monsoonal winds modulate convection near the Strait. Figure 4 displays a bimodal seasonal distribution of deep convection. Lightning is more frequent during April than October within the Strait. Minima near the Strait occur during July and February, with February having the least lightning. These results are consistent with the number of thunderstorm days at WMKK, the most representative airport in the region. The greatest seasonal variability in nighttime strokes is over the

Strait, similar to the daytime strokes on land, whereas the nighttime strokes over land are less variable. Small values of outgoing longwave radiation over the Strait during October and April are consistent with the results from the lightning data (e.g., Meehl 1987; Matsumoto 1993; Matsumoto and Murakami 2000, 2002).

The lightning maxima in Fig. 4 occur primarily during the monsoon transitional seasons of March through May (MAM) and September through November (SON). Conversely, the minima occur during the peak monsoon seasons of December through February (DJF) and June through August (JJA; e.g., Krishnamurti and Bhalme 1976; Meehl 1987; Hendon and Woodberry 1993; Matsumoto 1993; Oki and Musiake 1994; Wang 1994; Ju and Slingo 1995; Matsumoto and Murakami 2000, 2002; Chang et al. 2004, 2005; He et al. 2006, 2007). Figure 6 shows average streamlines and isotachs at 10 m during a) January, b) April, c) October, and d) July of 2005–2011. The low-level monsoonal winds are strongest during January and July when they can weaken or inhibit the mesoscale circulations described above (e.g., Leopold 1949; Estoque 1962; Pielke 1974; Arritt 1993).

The lightning maxima in Fig. 4 are linked to the passage of the ITCZ (e.g., Crowe 1951; Waliser and Gautier 1993; Aldrian and Dwi Susanto 2003; Sakurai et al. 2005; Aldrian et al. 2007; Berry and Reeder 2013). Maximum precipitation near the Strait occurs during October, with a secondary peak in April (Meehl 1987; Oki and Musiake 1994; Chang et al. 2005). Rain gauge data in the area, show the same seasonal bimodal distribution as Fig. 4, but with a stronger peak during October (Aldrian and Dwi Susanto 2003; Aldrian et al. 2007). The authors attributed this seasonality to the passage of the ITCZ.

Periods of maximum precipitation do not necessarily correspond to maximum lightning since instability and a mechanism to initiate convection is required for thunderstorm formation. Figure 7 shows average (2005–2011) convective available potential energy (CAPE) based on data from the Global Data Assimilation System (GDAS; Kanamitsu 1989). There

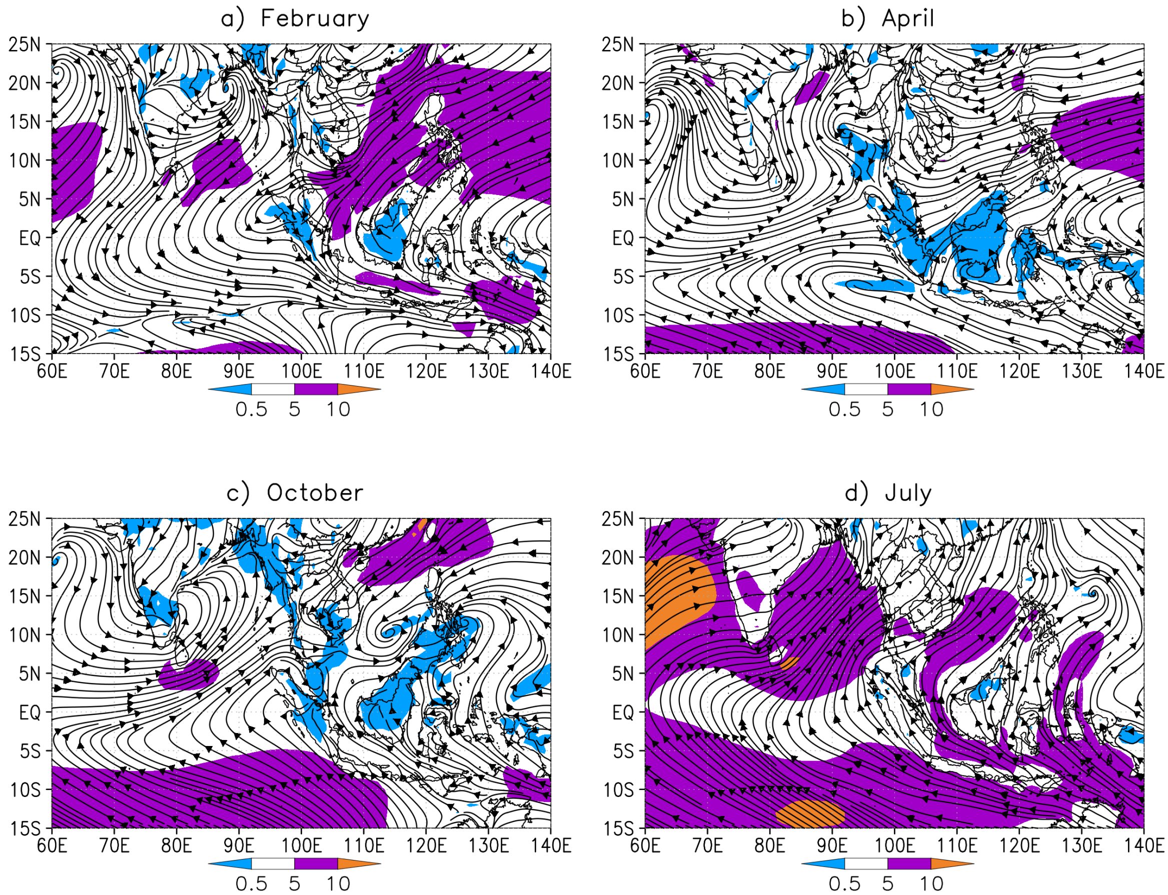

FIG. 6. GDAS analyses of 10 m winds [m s^{-1}] during a) February, b) April, c) October, and d) July. July is shown as a comparison of winds during the monsoon season.

is greater CAPE in the Strait during April than October. Oki and Musiake (1994) found that the intensity of precipitation was stronger in April on the west coast of Peninsular Malaysia. This is a direct reflection of the local instability and the resulting capability of storms to produce stronger updrafts which are associated with enhanced lightning. During April, winds within the Strait are weaker than during October (Fig. 6), and the combined influence of greater instability and lighter winds leads to a greater chance of deep convection from mesoscale circulations near the Strait (e.g., Leopold 1949; Estoque 1962; Pielke 1974; Arritt 1993).

To summarize, rain gauge data indicate that October is the peak rain month in the region of the Strait, while WWLLN lightning data show that April is the peak month for lightning (Fig. 4). The primary forcing mechanism for convection is the convergence of mesoscale circulations, including sea/land breezes, katabatic/anabatic winds, and rain-produced cold-air gravity currents. The convection within the Strait is a function of the convection over the surrounding landmasses the evening before (Fujita et al. 2010). The sea breeze initiates and propagates this convection, and both April and October are active sea breeze months Sakurai et al. (2005). Winds are stronger over the Strait during SON compared to MAM (Fig. 6). With lighter winds during MAM, the resulting enhanced mesoscale circulations over the Strait can combine to produce deep convection.

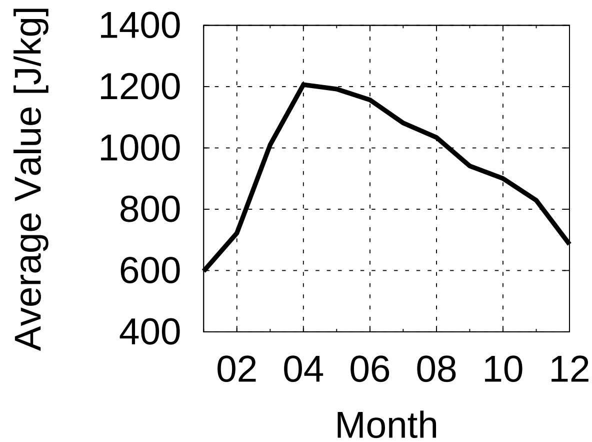

FIG. 7. Average (2005–2011) CAPE [J kg^{-1}] from the GDAS model for grid points within the Strait of Malacca.

1.3 Transport of ship emissions

The widespread deep convection within the Strait can produce long-range transport of the ship emissions that are present. Successfully modeling this transport greatly depends on the quality and resolution of the meteorological model used. High resolution modeling is especially important due to the complex topography of the region and the major role of mesoscale circulations in creating the deep convection. A finer grid spacing in the vertical can have varying, but mostly improved effects (Aligo et al. 2009). Horizontal grid spacing smaller than $\sim$6 km in models such as the Weather Research and Forecasting Model (WRF; Skamarock et al. 2008) can explicitly resolve convection. This means that the model can reasonably simulate a storm's updrafts, downdrafts, and other convective features. The term "explicit resolution" is used with the understanding that a grid spacing less than $\sim$1 km (i.e., a cloud resolving model [e.g., Weisman et al. 1997]) is needed to fully resolve the small-scale processes comprising the convection.

Models with horizontal grid spacing coarser than $\sim$6 km, such as the $\sim$27 km used in the GDAS model, implicitly resolve the net effects of convection at the scale of the model, not the individual convective components. Various cumulus parameterization schemes seek to simulate these net effects (e.g., Kain and Fritsch 1992; Grell and Dévényi 2002). Parameterizing convection is essential in global models because of their relatively coarse resolution. Inaccurately diagnosing convection can lead to major errors in pollutant transport (e.g., Jacob et al. 1997; Lin et al. 2010; Klich and Fuelberg 2013). Instead of emissions being quickly lofted to the upper atmosphere by convective updrafts where they can travel great distances, the emissions may remain at much lower altitudes where they interact with the surface and not travel as far (e.g., deposit too soon). Since most of the rainfall near the Strait is convective in nature (e.g., Schumacher and Houze 2003), accurately simulating deep convection is imperative to this study.

When utilizing off-line transport models, the grid resolution of the input meteorological data can make a major difference in the transport of emissions. The grid spacing of a model also determines its depiction of topography. Figure 8 compares the topographic resolution over the Strait between the $\sim$110 km (1°) GDAS data provided by the Air Resources Laboratory (ARL; described in Section 2.4) and a 2 km WRF simulation. The GDAS data (Fig. 8a) depict only large-scale features such as the mountain-strait-mountain structure of the region. However, small-scale features such as the irregular coastline and the overall shape of the mountains (peaks, valleys, and ridges) are not resolved due to the coarse grid spacing. Figure 8b shows the WRF Model topography. The mountain spine of each landmass is clearly visible, as are the coastlines, islands, and peaks, valleys, and ridges.

1.3.1 Transport using global models

Properly resolving small topographic features is important because they greatly influence the development of mesoscale circulations that can lead to deep convection near or over the Strait. For example, if a sea breeze initiates on the east coast of Sumatra when the environmental flow is calm, its movement with the GDAS topography primarily will be toward the southwest (i.e., perpendicular to the coast line, Fig. 8a). Conversely, in the higher resolution WRF Model (Fig. 8b), the sea breeze can propagate anywhere from northwest to south, depending on its exact location. In addition, on the west-central coast of the Malay Peninsula, the GDAS data's topography is concave toward the Strait, compared to the WRF Model whose topography predominately is convex toward the Strait. North and south of the GDAS feature are regions of convex topography toward the Strait. These can lead to areas of false convergence and divergence and misplaced convection, or earlier and heavier precipitation over land or water (e.g., Hara et al. 2009). The opposite can occur over the Strait at night, leading to misplaced convection that can transport simulated particles incorrectly.

The distribution of storm tops within the Strait has not been reported to the author's knowledge. However, typical tropical deep convection can reach 20 km (Folkins and Martin 2005; Wissmeier and Goler 2009). The parameterization schemes of coarse resolution models typically greatly underestimate these heights (Lin et al. 2010). Therefore, the simulated convection in the Strait may not be sufficiently strong or tall, which will greatly modify the simulated transport of emissions.

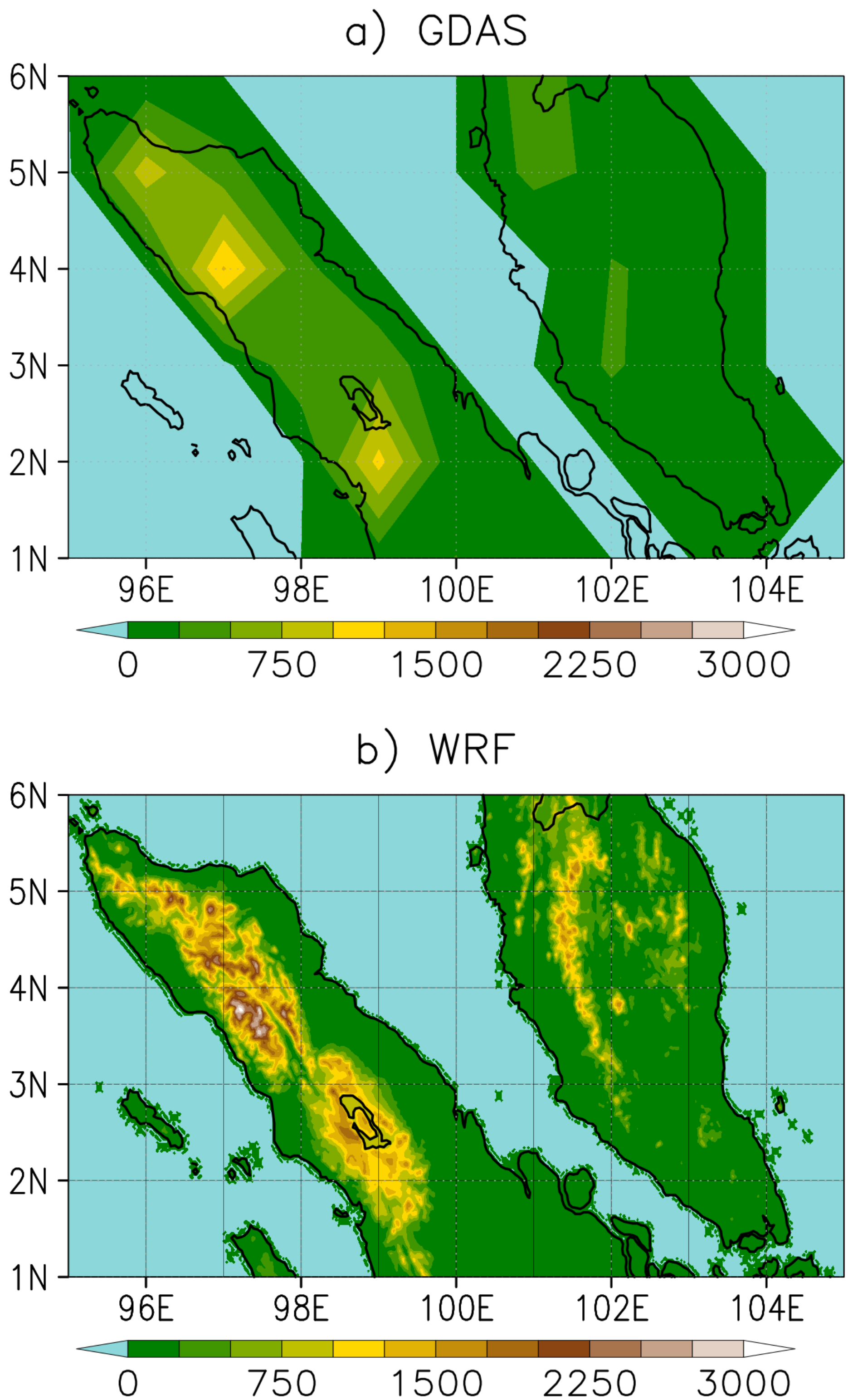

FIG. 8. Comparison of terrain height [m] between the a) GDAS and b) WRF models.

The long range transport of ship emissions usually has been simulated using Global Chemical Transport Models (GCTMs; e.g., Capaldo et al. 1999; Lawrence and Crutzen 1999; Davis et al. 2001; Endresen et al. 2003; Dalsøren et al. 2009). The simulations typically extend over one or more months and are at low spatial resolution. For example, Endresen et al. (2003) used 5.6° × 5.6° grid spacing. This coarse resolution would not adequately simulate the Strait's contribution to global ship emissions. A higher resolution global transport model used by Lawrence and Crutzen (1999) used 2° × 2° grid spacing, while Dalsøren et al. (2009) used 1.8° × 1.8° spacing. These latter, somewhat higher-resolution models would simulate a small contribution from the Strait, but with minimal detail. Without the use of even higher resolution regional models, accurate representation of ship emissions is insufficient.

1.3.2 Transport using regional models

Regional transport models can be run at higher resolution than global models and therefore can produce more realistic simulations of mesoscale phenomena (Lin et al. 2010; Klich and Fuelberg 2013). The regional studies by Streets et al. (1997) and Streets et al. (2000), mentioned earlier, utilized 1° × 1° grid spacing over Southeast Asia. Their results showed that ship emissions within the Strait could contribute significantly to sulfur deposition on the nearby land. Streets et al. (2000) were partially able to resolve the sea breeze and enhanced precipitation over Sumatra, coastal Malaysia, and Singapore. However, there was no mention of the land breeze and subsequent long-range transport via deep convection.

Also relevant to this study is the high-resolution modeling of meteorological conditions and subsequent pollutant transport over Mexico City (e.g., de Foy et al. 2009). Mexico City lies in a basin enclosed by mountains on three sides. Its up- and down-slope winds are a diurnal feature similar to those within the Strait. Nested WRF simulations, with grid spacing as small as 3 km, simulated a recirculation mechanism that produced a slow removal of pollutants on actively convective days (de Foy et al. 2009).

To summarize, the majority of previous ship emission studies used GCTMs. None have focused on the regional transport of ship emissions from the Strait using a regional transport model. The coarse resolution models either poorly depict the various mesoscale phenomena discussed above, or perhaps not at all. However, higher resolution models can resolve the mesoscale features that are important in a complex region such as the Strait. Coarse resolution models parameterize convection, ignoring the individual convective components, whereas a high-resolution model will simulate them more realistically. Poor representation of convection and its precursors will adversely affect the simulation of long-range pollutant transport.

1.4 Objectives

The objective of this research is to describe and quantify the horizontal and vertical transport of ship emissions in the Strait of Malacca using high-resolution modeling. Differences in the long range transport of ship emissions between high- and low-resolution models also will be described. Trajectories will be released in the Strait using both the low- and high-resolution meteorological conditions provided by the GDAS and WRF models, respectively. Chapter 2 describes the data and methodology used to simulate trajectories in the Strait. Chapter 3 discusses results, and a summary is provided in Chapter 4.

CHAPTER 2

DATA AND METHODS

2.1 Study periods

This study focused on two months when deep convection was most active within the Strait, April and October, and on February because of its relatively small amount of deep convection (Fig. 4). Since the observed convection during any 5-day period is not much different from that before or after, the 14$^{\text{th}}$ day (0000 UTC) of each of the three months during 2011 was randomly selected as the start of each study period. The periods ended at 0000 UTC on the 21$^{\text{st}}$ day of each month. No tropical cyclones or deep convective cloud clusters passed directly over the Strait during these periods. However, satellite imagery shows several systems did form at more distant locations, although they appeared to have no influence on conditions within the Strait.

2.2 WWLLN data

Data from the WWLLN were used to locate lightning and determine its spatial patterns in the study region. The WWLLN is a worldwide network of over 50 VLF (3–30 kHz) sferic sensors. In the region of the Strait, the WWLLN's location accuracy is between 10 and 30 km (Fig. 5 of Rodger et al. 2009), and its detection efficiency is ~12–16% (Fig. 13 of Rodger et al. 2006). Since additional WWLLN sensors were added since the publication of Rodger et al., the network's detection likely has improved somewhat (e.g., Hutchins et al. 2012). Nonetheless, the lightning reported in Figs. 3, 4, and 5 underestimates the actual amount that occurs. Although the location accuracy and detection efficiency are not as good as those of denser networks such as the National Lightning Detection Network (Orville 2008), this should not affect the distinct patterns observed over the region, only the number of strokes detected.

2.3 HYSPLIT

2.3.1 Model specifics

The HYbrid Single Particle Lagrangian Integrated Trajectories model (HYSPLIT_4; Draxler and Hess 1997) was used to calculate forward trajectories of particles released near the surface. HYSPLIT has been used extensively in both global and regional pollutant transport studies (e.g., McGowan and Clark 2008; Wang et al. 2010; Klich and Fuelberg 2013). The HYSPLIT calculations are a hybrid between Eulerian (concentrations) and Lagrangian (advection and diffusion) approaches. "The time integrated advection of each particle can be viewed as a simple trajectory which only requires the three-dimensional wind field" (Draxler and Hess 1997). Output from the WRF (high resolution) and GDAS (coarse resolution) meteorological models separately provided the three-dimensional wind fields needed by HYSPLIT. HYSPLIT linearly interpolates these data from the input models' vertical coordinate system into its own terrain-following (σ) coordinate with no loss in horizontal resolution. A trajectory was terminated when it left the study domain. If a trajectory hit the surface, it was either advected along the surface until the integration was complete (provided it remains in the domain), or was subsequently lifted above the surface by downstream vertical motion. When using nested domains (such as the WRF simulations here; discussed later), HYSPLIT allows a trajectory to pass freely between the domains, but always uses the finest resolution data available.

2.3.2 Particle release specifics

Three thousand, randomly placed particles (in x, y, and z) were released simultaneously every hour, during the first 48 h (0000 UTC on the 14^{th} through 2300 UTC on the 15^{th} of each month), within the horizontal confines of the Strait (as defined in Fig. 4). A combination of ArcGIS's "Create Random Points" tool and Python assigned the random coordinates for the released particles. All trajectories were forward, and terminated 120 h after release. The releases occurred between the altitudes of 10 and 500 m, since the depth of the marine boundary layer in the area typically is ∼500 m (e.g., Satyanarayana et al. 2000; Sam et al. 2003), and ship emissions usually are confined within this layer in the absence of deep convection (e.g., Liu et al. 2000; von Glasow et al. 2003; Chosson et al. 2008; Eyring et al. 2010). Observations have shown that the major ship traffic virtually continuously pollutes the Strait (e.g., Fig. 2; Beirle et al. 2004; Richter et al. 2004; Franke et al. 2009). Therefore, emissions from one time combine with those from another time forming a mixture of recent and older pollutants (Eyring et al. 2010, and references therein).

2.4 GDAS meteorological data

Both high- and low-resolution trajectories were calculated using HYSPLIT. The low-resolution version was run using meteorological data from the National Centers for Environmental Prediction's (NCEP) GDAS model (aka package) obtained from the archive of the National Oceanic and Atmospheric Administration's (NOAA) Air Resources Laboratory (ARL). The GDAS package is a three-dimensional variational data assimilation (3DVAR) system that assimilates observed data from sources such as radiosondes, satellites, aircraft, buoys, radars, and ships. These assimilated data provide the initial conditions for NCEP's Global Forecast System (GFS; McPherson et al. 1979; Kistler and Parrish 1982; Kanamitsu 1989; Kleist et al. 2009). The GFS is a T574 (∼27 km, since 22 June 2010) spectral model with 64 hybrid sigma-pressure vertical levels (T574L64). The GDAS package is run four times per day, at 0000, 0600, 1200, and 1800 UTC, with the previous GFS run, with additional analyses (the Final [FNL] analysis), providing the initial conditions. Post-processing procedures convert the data from the native GFS resolution to coarser resolution for public use. The ARL further converts the post-processed GDAS data for input to HYSPLIT. These data have a grid spacing of $1^\circ \times 1^\circ$ (360×181 grid cells) in the horizontal, 23 pressure levels in the vertical, and a temporal resolution of 3 h. This ARL dataset is the source of the meteorological data within this paper and provided the meteorological conditions for the coarse-resolution forward trajectories.

2.5 The WRF Model

The WRF Model Version 3.5 (Skamarock et al. 2008), with the Advanced Research WRF (ARW) core, was used to obtain meteorological fields for the high-resolution HYSPLIT trajectories. Initial and boundary conditions were from FNL analyses (a product of the GDAS) with a $1^\circ \times 1^\circ$ grid spacing. The WRF computational domain consisted of three, two-way nested regions (Fig. 9). The outer domain (d01), with a horizontal grid spacing of 18 km, depicted synoptic-scale features. Domain 2 (d02) had a horizontal grid spacing of 6 km. It was the intermediary between d01 and Domain 3 (d03). Domain 3 had a 2 km grid spacing. Centered over the Strait, its high-resolution grid spacing captured most aspects of the various mesoscale processes that are important to deep convection. All three domains had 50 vertical levels, with a large number located in the boundary layer. The spacing of the levels varied, with those in the boundary layer ranging from 50–150 m, and those in the lower, middle, and upper troposphere/lower stratosphere (UTLS) ranging from approximately 200 to 5000 m. Simulations were initialized at 1200 UTC on the 13$^{\text{th}}$ and

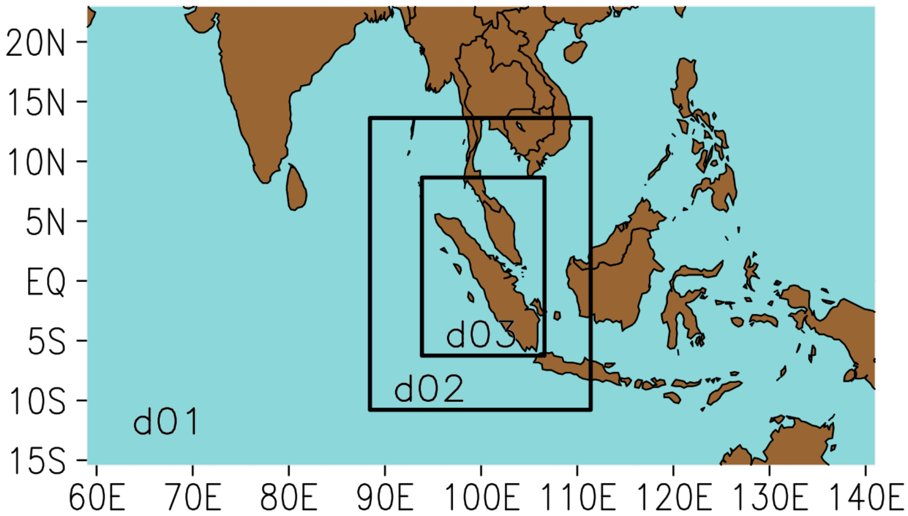

Fig. 9. WRF computational domain. The outer domain (d01) has a horizontal grid spacing of 18 km. Domain 2 (d02) has a horizontal grid spacing of 6 km, and Domain 3 (d03) has a 2 km grid spacing.

run through 0000 UTC on the 21st of each study month. The first 12 h were considered as a "spin-up" period and not used in the trajectory calculations.

Temperature, moisture, and horizontal winds above the boundary layer in d01 were nudged to the FNL analyses every 6 h for the duration of the integration. The objective was to keep the large-scale winds (and subsequent long-range transport) consistent with the analyses.

A suite of well-known procedures was used to parameterize various physical processes in the WRF simulations (Table 1). Less well-known settings within the simulations included terrain-slope effects on radiation (slope_rad) and topographic shading (topo_shading; with a shadow length of 25 km [shadlen]). Also included was a full diffusion option (diff_opt) that evaluates mixing terms in physical space using a horizontal Smagorinsky first-order closure turbulence parameterization (km_opt; the PBL scheme diffuses vertically). Diffusive damping (damp_opt) was employed within 1 km of the model top (zdamp). An adaptive time step maintained numerical stability. Convection was explicitly resolved in d02 and d03 (grid spacing of 6 km and 2 km, respectively). Thirty arc second geographic data represented topographic features. The WRF Preprocessing System simplified and scaled the data to the grid spacing of each domain. Therefore, the 30" geographic data were converted to a spacing of 2 km in d03 (Fig. 8b), 6 km in d02, and 18 km in d01.

Table 1. WRF Version 3.5 model parameters.

Namelist Variable	**Option**	**Reference**
cu_physics	Grell-3	Grell and Dévényi (2002) (improved)
bl_pbl_physics	YSU	Hong et al. (2006)
mp_physics	Lin (Purdue)	Lin et al. (1983)
ra_sw/lw_physics	RRTMG (15-min update)	Iacono et al. (2008)
sf_sfclay_physics	MM5 Monin-Obukhov	Monin and Obukhov (1954)
sf_surface_physics	Unified Noah Land-Surface	Tewari et al. (2004)

2.5.1 Verification of the WRF Model simulations

Characteristics of the simulated deep convection and sea/land breezes over the Strait region were compared to those discussed in Section 1.2.1 to test model performance. Figure 10 displays WRF simulated maximum reflectivity and 10 m winds, with superimposed WWLLN data, on 15 October 2011. It is typical of the many convective days during the study period. The WWLLN data were summed and binned within a ± 15 min window around each hour. For example, if WWLLN recorded a stroke at 12:49:00 UTC, it was counted as a stroke that occurred at 13:00:00 UTC. Only 50% of WWLLN data for the time period were used to isolate strokes occuring near the hour. Using less than 15 min gave insufficient detail, while greater than 15 min was too far from the hour. Figure 10a, at 1000 LT 15 October, displays a recently formed sea breeze (red arrows). The sea breeze intensifies and propagates inland where convection begins to develop over the mountains of both landmasses (Fig. 10b). Figure 10c shows the time of maximum deep convection over the landmasses, and Fig. 10d shows the splitting and subsequent propagation of the deep convection toward the coasts. The land breeze (green arrows) and outflow boundaries (blue arrows) at this time are readily visible. By 0000 LT (Fig. 10e), the coupled deep convection-land breeze system propagates offshore and begins to develop new convective cells in the convergence zone near the middle of the Strait. The most intense convection within the Strait occurs between ~0100–0800 LT, with the maximum for this study period at 0300 LT (Fig. 10f). The figure dramatically illustrates the complex nature of the mesoscale forcing mechanisms associated with the deep convection and the model's ability to resolve them. Locations of observed lightning on this day agree closely with the simulated locations and timing of deep convection.

The location and timing of every convective cell on 15 October 2011, or any other simulation day, obviously will not correspond exactly to the WWLLN observations. The other simulation days that were examined exhibited similar degrees of agreement with typical conditions (not shown). Nonetheless, the degree to which WRF simulated convection in the Strait agrees with typical conditions, renders the simulations appropriate for the research that follows. Ideally, higher resolution observations for verification were preferred, but satellite and radar observations of the region were insufficient. Therefore, WWLLN observations provided enough information to diagnose accurately placed convection.

2.6 EDGAR emissions data

Ships are not major emitters of CO compared to other anthropogenic sources (Endresen et al. 2003; Eyring et al. 2005); however, CO is a convenient species to study because of its long residence time (1–2 mo) and widespread use in previous transport studies (e.g.,

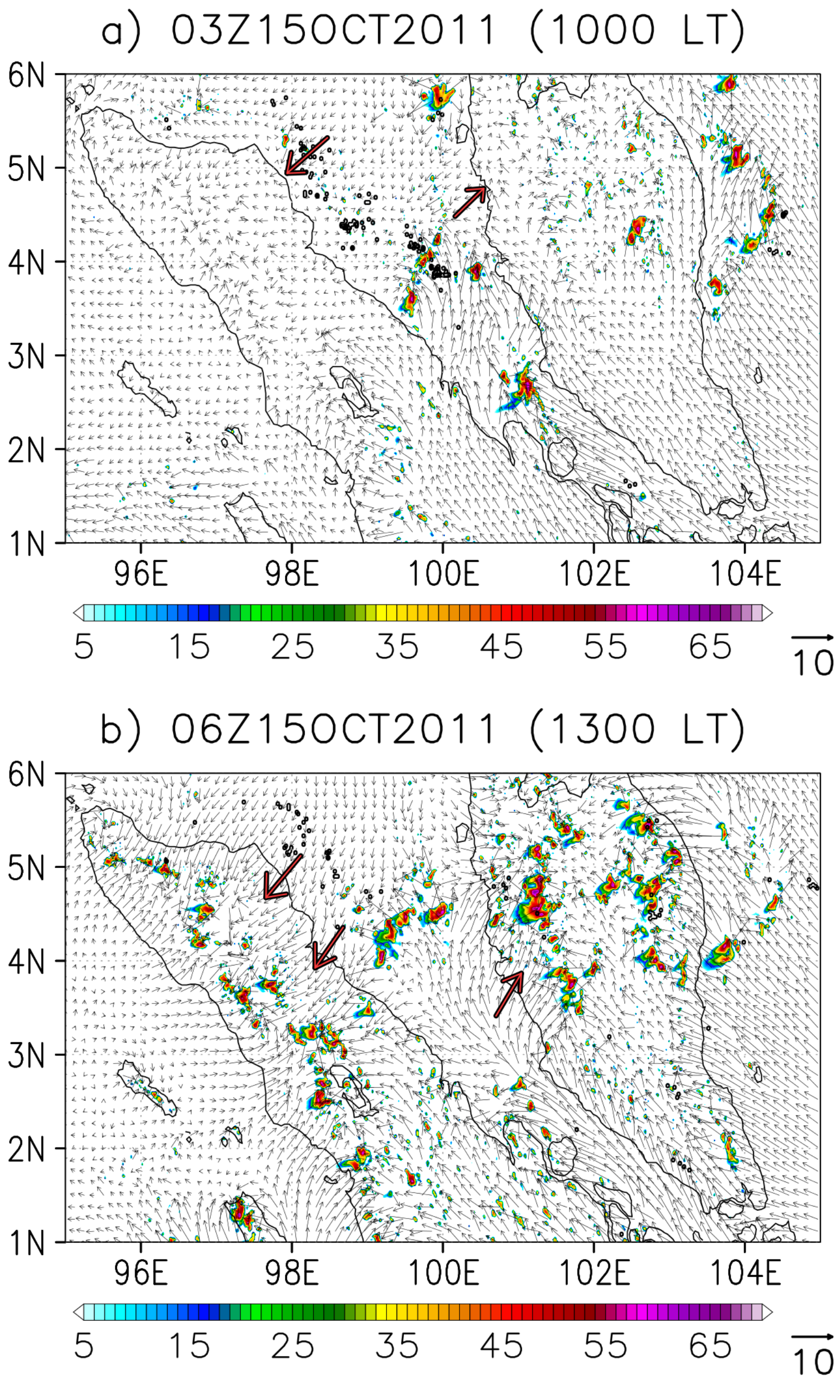

FIG. 10. The WRF model simulation characteristics of deep convection development and propagation in the Strait region. Winds [m s^{-1}] are shown at an interval of 14 km (7 grid cells). The color scale represents simulated maximum reflectivity [dBZ], and black contours represent WWLLN lightning observations. Red arrows represent sea breeze propagation, green arrows represent land breeze propagation, and blue arrows represent outflow boundaries associated with the convection.

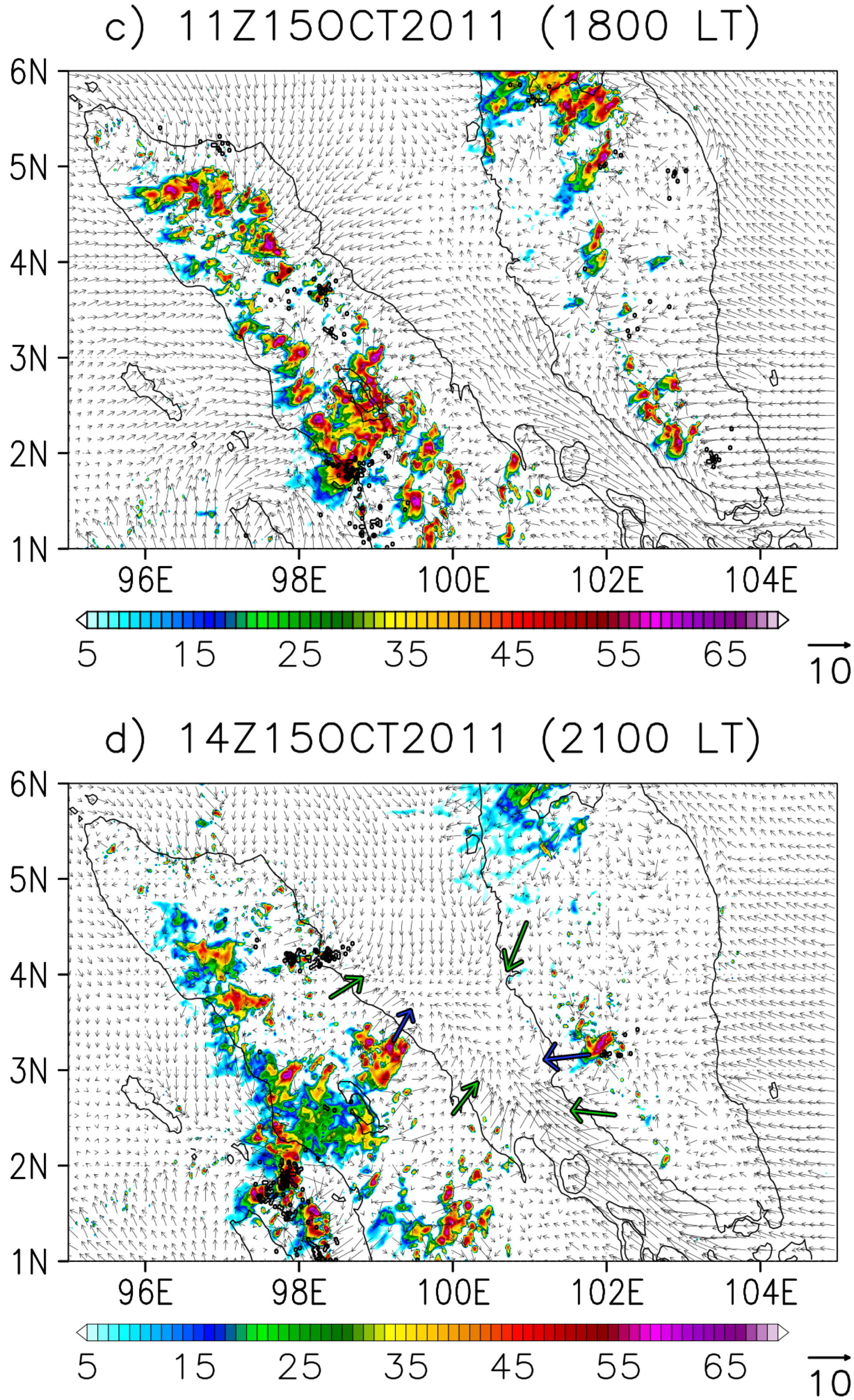

Fig. 10. (Continued).

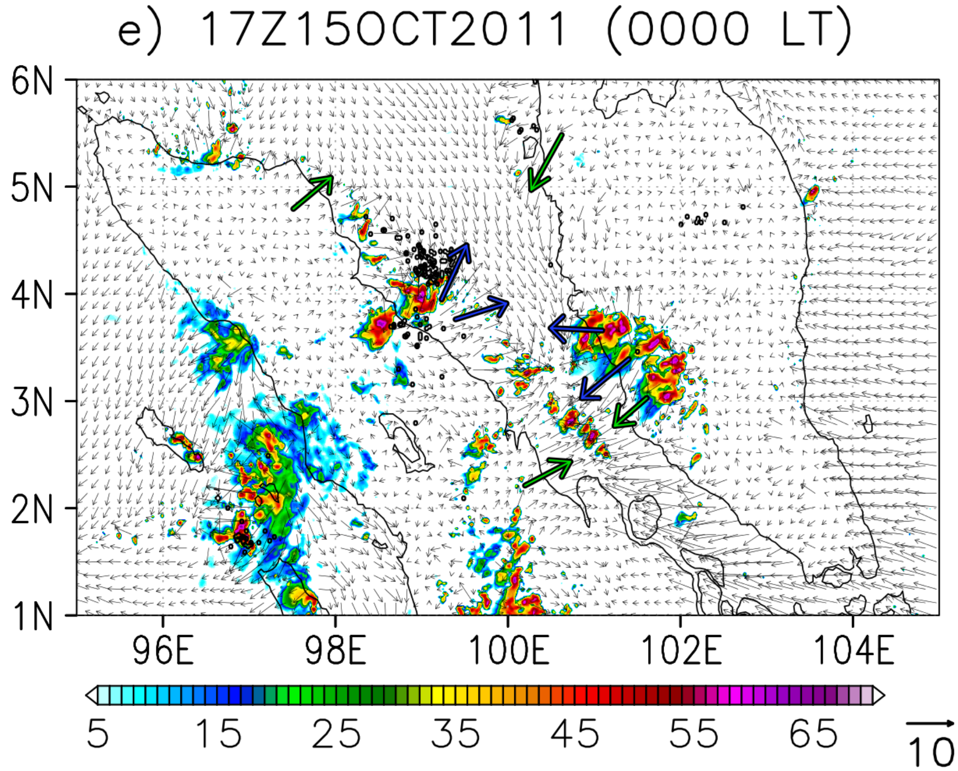

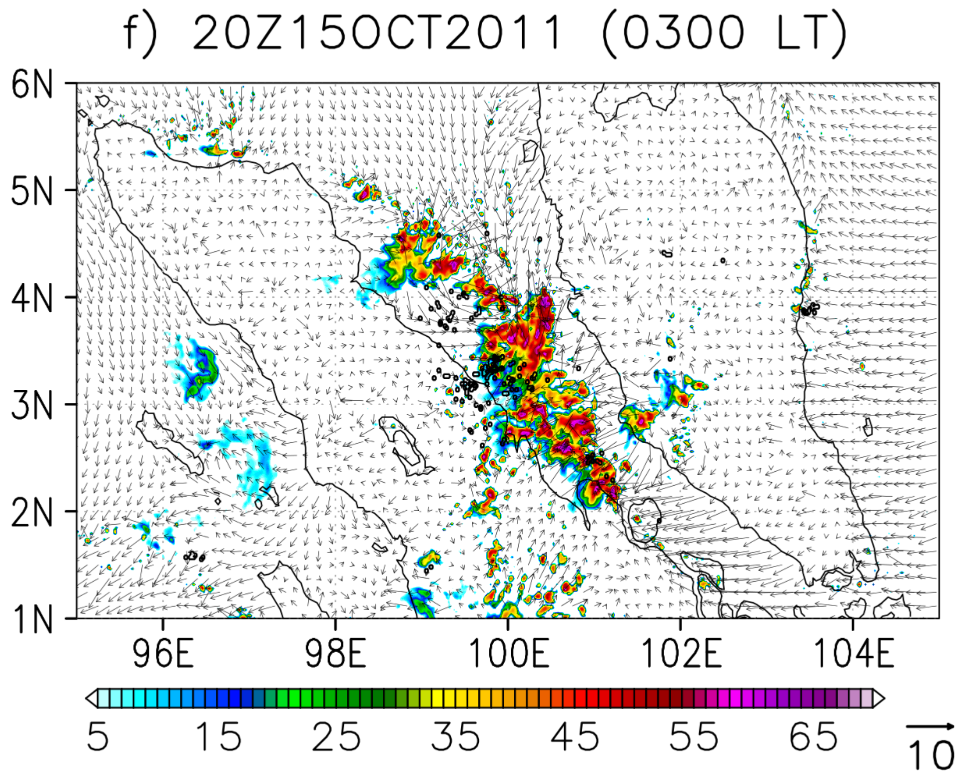

Fig. 10. (Continued).

Novelli et al. 1998; Klich and Fuelberg 2013). Species such as NO_x and SO_2 are more difficult to quantify using a passive-tracer method such as HYSPLIT (e.g., Hane 1978; Hales and Dana 1979; Mari et al. 2000; Wang and Prinn 2000; Ridley et al. 2004; Grooß and Russell III 2005) because they interact with water and other molecules on a much faster time scale than CO.

The Emission Database for Global Atmospheric Research Version 4.2 (EDGAR; online at http://edgar.jrc.ec.europa.eu/), with the "non-road transportation" sub-dataset, was used to determine the emission rate of CO. The major shipping lane within the Strait is near Indonesia with minor lanes branching from it (similar Fig. 2). The average emission rate was determined to be 4.1 t CO 0.01 deg^{-2} yr^{-1} within the Strait, corresponding to 3.76×10^{-6} t CO km^{-2} h^{-1}. As mentioned previously, 3000 trajectories were released within the Strait every hour during the first 48 h of a study period. Assuming the area of the Strait to be $\sim 58.9 \times 10^3$ km^2 yields an emissions rate of 0.22 t CO h^{-1}. Division by 3000 particles h^{-1} and conversion to grams yields 66.22 g CO per particle released.

CHAPTER 3

RESULTS

3.1 Winds

The large scale, low-level winds in the study region are greatly modified by the local terrain. These local winds during the three study periods are described in detail in the following section. Comparisons are made between the high resolution depictions provided by WRF and those by the coarser resolution GDAS. Deviations from the low-level average monthly conditions shown in Fig. 6 are shown where appropriate. One should note that the streamline analyses do not represent trajectories of air parcels. The trajectories are described in a later section.

3.1.1 Low-level winds

Figure 11 shows average study-period (0000 UTC 14$^{\mathrm{th}}$ day through 0000 UTC 21$^{\mathrm{st}}$ day) WRF- and GDAS-derived winds at 10 m for each study period. The higher resolution WRF model (d01: 18 km grid spacing) winds during April (Fig. 11a) over the South China Sea (Indian Ocean) are primarily easterly (westerly) at speeds between 0.5 and 5 m s^{-1}, and are similar to those of climatology (Fig. 6b). Within the Strait itself, the winds flowing over each landmass's mountains and into the Strait, combine with the flow around the Titiwangsa Mountains to the north to create a cyclonic (convergent) flow with speeds < 5 m s^{-1}. This cyclonic structure within the Strait is indicative of the persistent convergence associated with the diurnal cycle that occurs there. Winds from the coarser GDAS data ($\sim$110 km grid spacing; Fig. 11b) are similar to those from WRF in direction and magnitude throughout the region, except north of Sumatra, where the aforementioned easterly and westerly flows meet.

WRF-derived, average study-period wind speeds during October over the Indian Ocean and South China Sea are between 0.5 and 5 m s^{-1} (Fig. 11c). Within the Strait, winds are generally < 0.5 m s^{-1}, with primarily southeasterly flow in the southern region, and northeasterly flow in the northern region. GDAS-derived winds (Fig. 11d) agree closely with those from WRF. GDAS is slightly more representative of climatology than WRF (Fig. 6c).

The February study period is characterized by much stronger winds near the Strait and throughout the South China Sea (Fig. 11e). Over the South China Sea, WRF-derived study-period average speeds are between 5 and 10 m s^{-1} near the coast of the Malay Peninsula and > 15 m s^{-1} off the southeast coast of Vietnam. Winds are primarily northerly over the western Indian Ocean (between 0.5 and 5 m s^{-1}) and westerly to northwesterly, ranging from 0.5 m s^{-1} in the west to > 10 m s^{-1} south of Sumatra. Flow within the Strait is primarily toward the south, combining with the southward-moving flow over the South China Sea. Wind directions from the GDAS data (Fig. 11f) agree well with those from WRF (with WRF having a more detailed mesoscale structure than GDAS); however, GDAS wind speeds over the western coast of the Malay Peninsula and Barisan Mountains are slightly weaker than those from WRF. The synoptic-scale patterns are similar to those of climatology (Fig. 6a), but wind speeds in the jet south of Java are considerably stronger than climatology in both models.

3.1.2 Mid-level winds

The mid-level (5 km) WRF-derived winds during April are primarily easterly over most of the region with speeds < 5 m s^{-1} (Fig. 12a). Near the equatorial Indian Ocean,

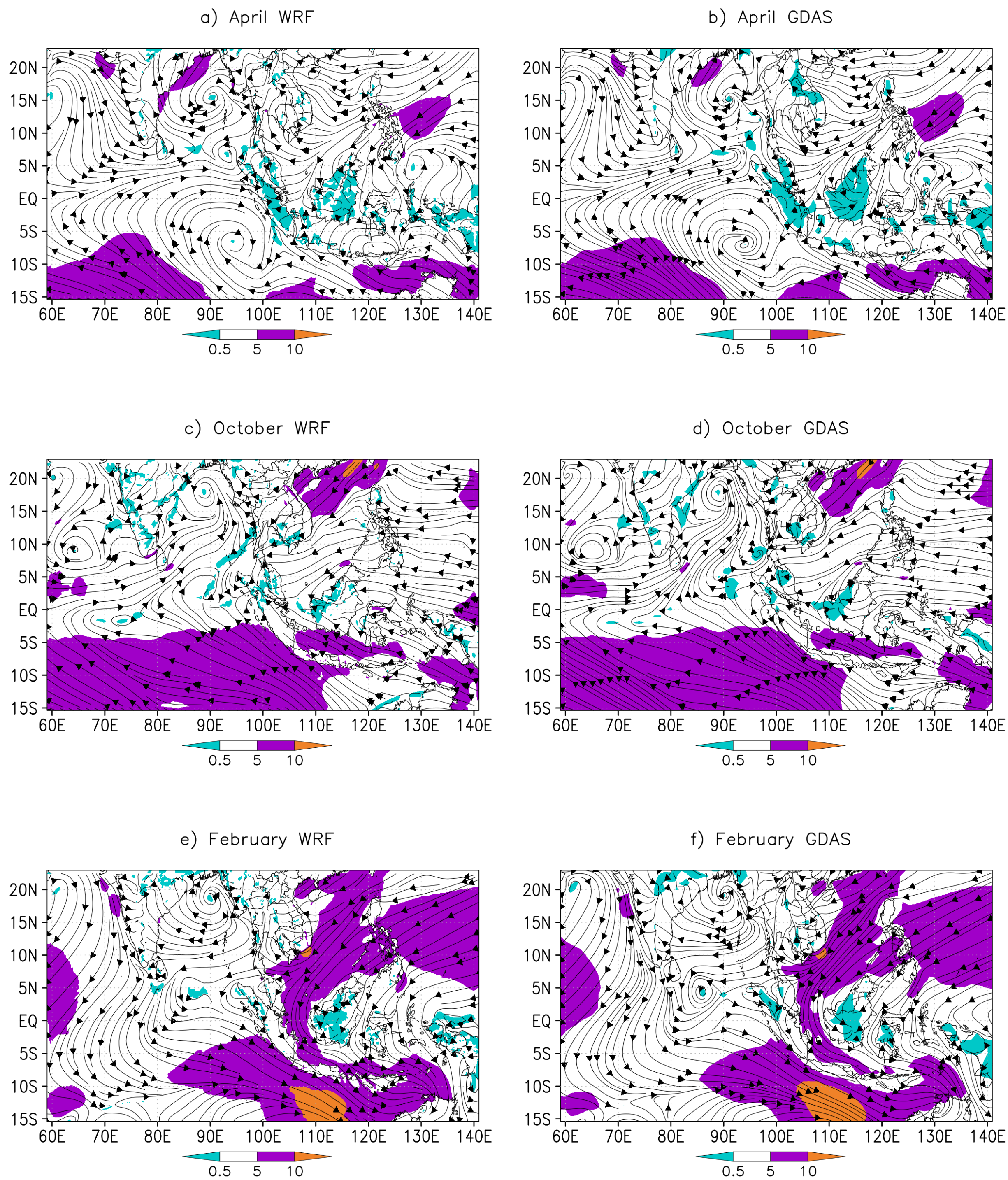

FIG. 11. Average 10 m winds from WRF (left) and GDAS (right) data during the three study periods (0000 UTC 14th day through 0000 UTC 21st day) of (a and b) April, (c and d) October, and (e and f) February 2011. Streamlines are thinned for the WRF-derived winds to better display the data.

winds are westerly, with speeds between 0.5 and 5 m s^{-1}. During October (Fig. 12c), winds are primarily easterly between ∼12° S and 7° N with speeds between 5 and 10 m s^{-1}. Section 3.2 will show that the stronger October winds cause trajectories originating over the Strait to travel faster than during any other month. During February (Fig. 12e), the Strait is a transitional zone between northern- and southern-hemisphere anticyclonic flows. Wind speeds are stronger than during April, at 0.5–5 m s^{-1} throughout the Indian Ocean between the Equator and 10° N, and 5–10 m s^{-1} over the Strait and South China Sea.

Winds from the GDAS data at 500 hPa mimic those from the WRF model (Figs. 12b, d, f). This occurs because winds above the PBL in the outer domain of WRF were nudged to FNL analyses every 6 h. The only major difference is during February (Fig. 12f) over the western Indian Ocean: GDAS anticyclonic flow extends farther west than in WRF. Winds from both models compare well to climatology (not shown).

3.1.3 Upper-level winds

The WRF-derived winds in the upper levels (12 km) are primarily easterly between 10° N and 10° S during all three study periods (Fig. 13) and resemble climatology (not shown). However, deviations from this easterly pattern occur west of 80° E during April (Figs. 13a, b) where winds become westerly. The next section will show that this flow pattern causes trajectories originating over the Strait to divert north or south from their westward orientation. During October (Figs. 13c, d), the Tibetan anticyclone is retreating eastward toward the Pacific and is located over Myanmar. This promotes easterly flow, with speeds of ∼10–20 m s^{-1} over the Strait and Indian Ocean. Conversely, during April and February (Figs. 13e, f) the anticyclone persists over the western Pacific Ocean. This leads to east-southeasterly flow over the Strait, southerly flow from southern India to Vietnam, and westerly flow near the northern regions of the domain. Flow over the Indian Ocean near

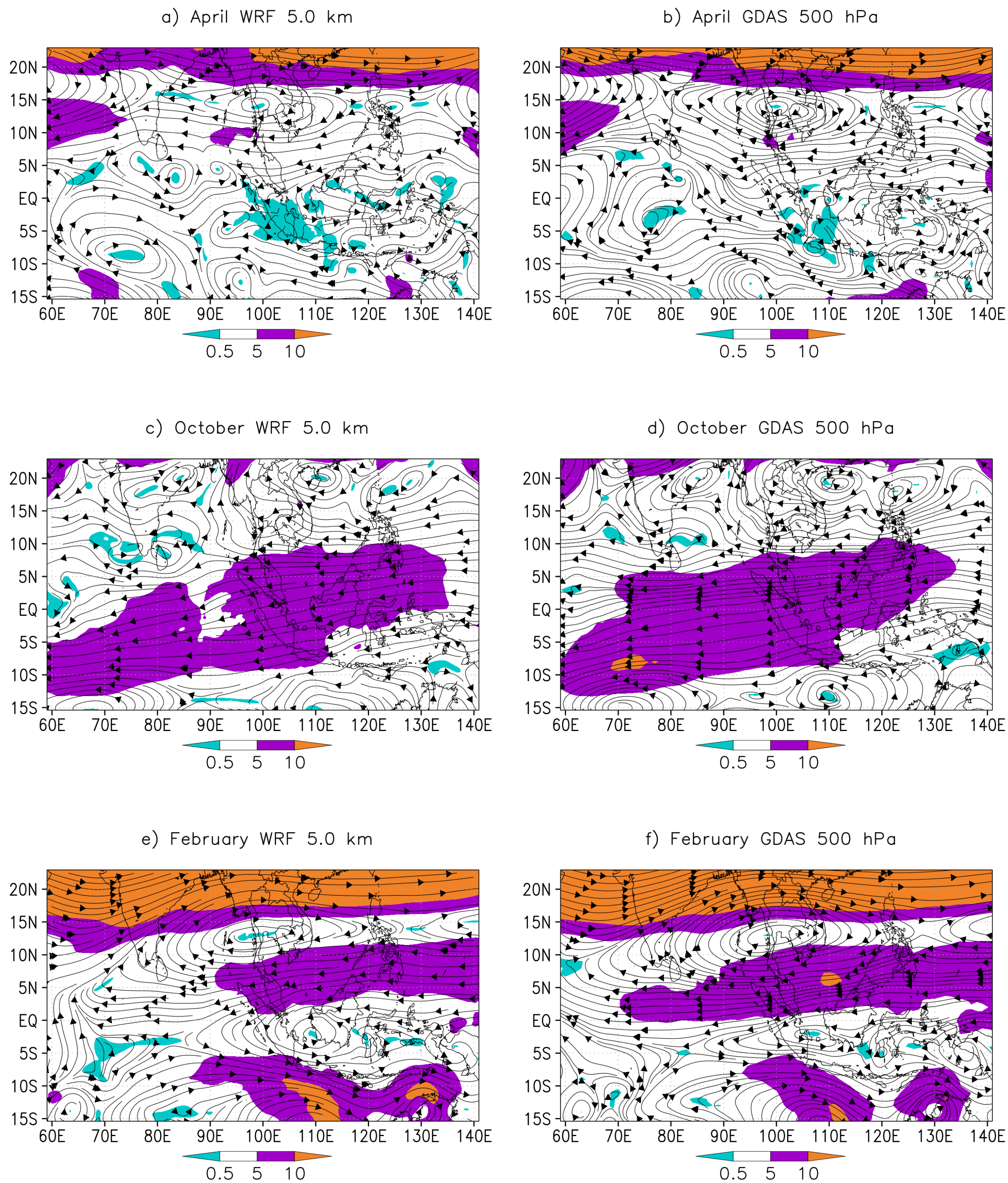

FIG. 12. As in Fig. 11, but for mid-level winds.

80° E during April switches from zonal to meridional, inhibiting trajectories from reaching the western edge of the domain.

The GDAS-derived winds at 200 hPa (Fig. 13, right column) show similar characteristics to the WRF-derived winds (Fig. 13, left column), including the westerly flow over the western Indian Ocean and the movement of the anticyclone. This again occurs because winds above the PBL in the outer domain of WRF were nudged to FNL analyses every 6 h.

3.1.4 Vertical wind profiles

Figure 14 shows profiles of average vertical motion for those grid cells containing 15 mm h^{-1} or more of either grid-scale (WRF) or convectively-parameterized (GDAS) precipitation. The GDAS results are averages for the years 2005–2011 since there were insufficient samples during the 2011 study periods alone. Nonetheless, the two profiles are considerably different. The WRF results are more realistic than GDAS results, showing a mid-tropospheric upward maximum over a thinner layer of downward motion (e.g., Golding 1993; May and Rajopadhyaya 1999; Heymsfield et al. 2010). The low-level, negative vertical motion is a result of the rain within the grid cell. Conversely, the GDAS results display upward vertical motion throughout the entire layer. The WRF model results show that April has the deepest and strongest layers of upward and downward motions, consistent with the enhanced lightning and instability shown in Figs. 4 and 7, respectively. Outside of April, February's largest upward maximum is located at $\sim$5–8 km, whereas the October maximum is > 8 km. The downdraft maximum is at $\sim$1 km for the WRF simulations. Overall, WRF-derived vertical motions in convective cores are stronger than those from GDAS. For instance, during April, WRF-derived vertical motions are $\sim$3.5 km h^{-1}, whereas GDAS-derived vertical motions are $\sim$0.2 km h^{-1}.

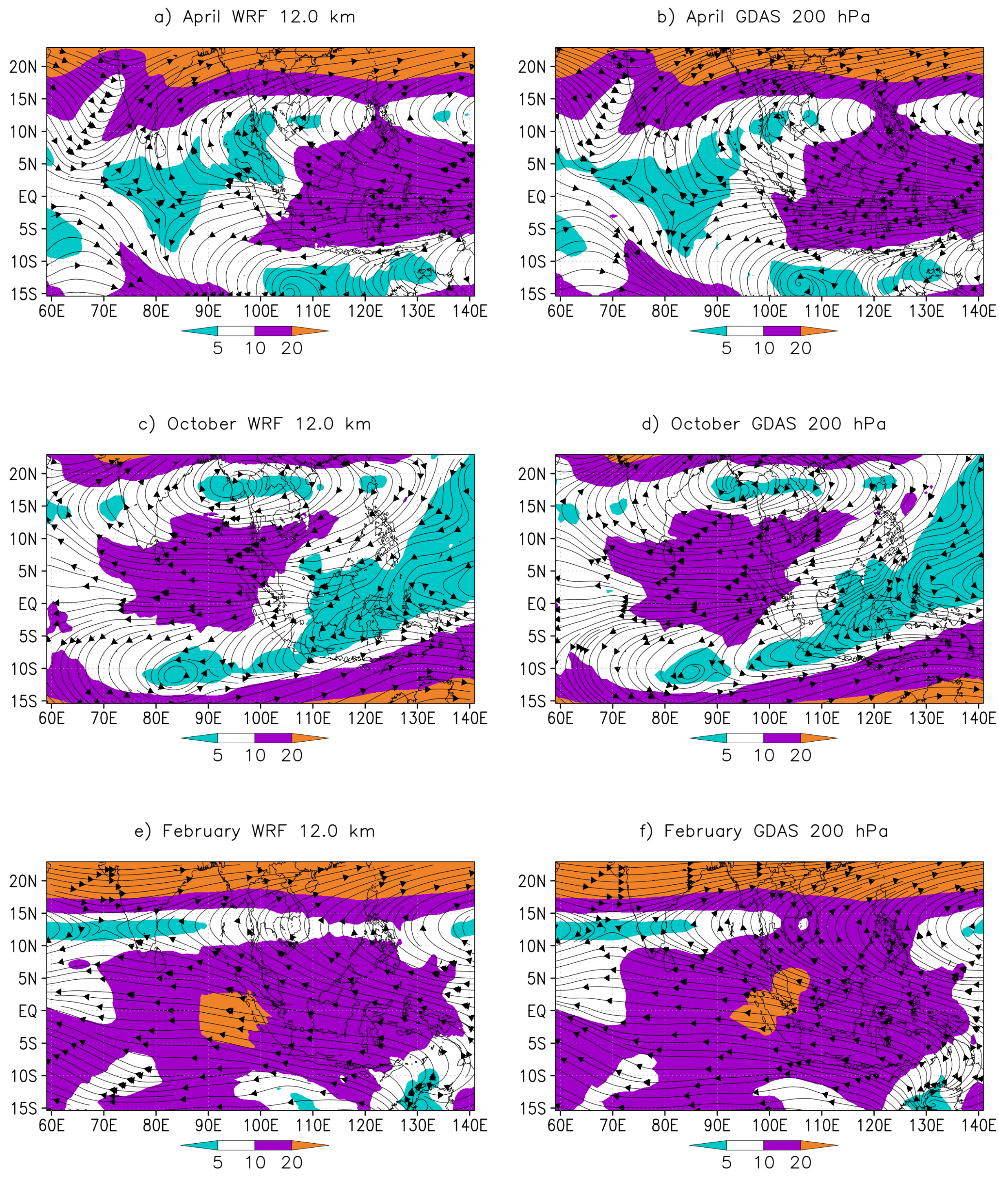

FIG. 13. As in Figs. 11 and 12, but for upper-level winds.

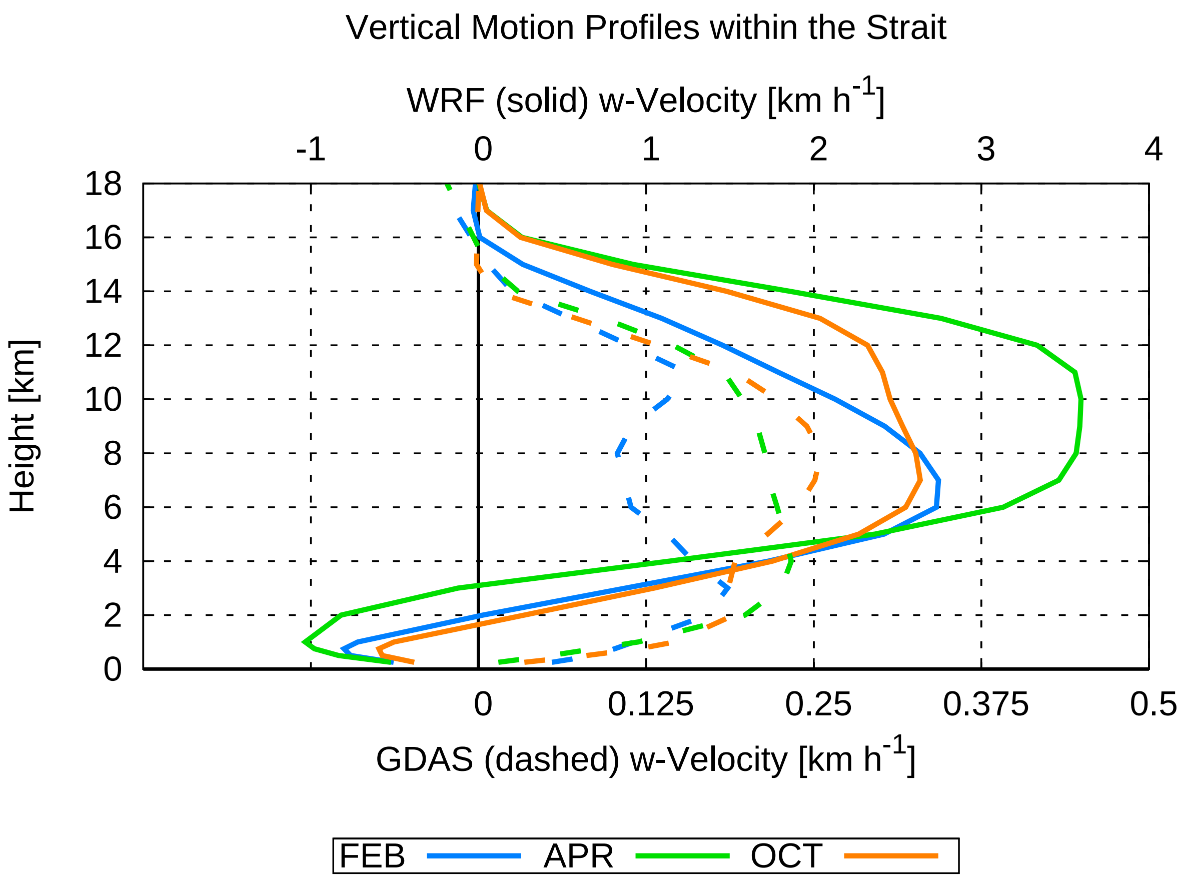

FIG. 14. Vertical motion profiles for WRF (solid) and GDAS (dashed) at grid points having at least 15 mm h^{-1} precipitation rate. Thresholds were selected based on grid-scale (convective parameterization) precipitation within WRF (GDAS). Vertical grid spacing is 1 km.

It is important to note that the GDAS-derived vertical motions are considerably smaller than those of WRF. This is partially due to the fact that the converted GDAS data files essentially omit data, which reduces the vertical velocities. This will modify the accuracy of the vertical extent of the trajectories. Contrary to WRF, October has the greatest upward vertical motion at ∼11 km. April has the greatest upward vertical motion at ∼7 km and above 14 km. Precipitation thresholds larger than 15 mm h^{-1} have convective cores characterized by greater positive ascent and descent, regardless of model (not shown).

3.2 Trajectory analysis

Figures 15–17 show the horizontal and vertical ending locations of forward trajectories released from the Strait (CO proxy; in pptv) after 120 h during April, October, and February 2011. Each released HYSPLIT particle corresponded to the prescribed mass of 66.22 g CO as described in Chapter 2. The particles were counted within the same $0.25° \times 0.25° \times 1$ km grid cells whether they were based on the WRF or GDAS data. Immediately apparent each month is the more extensive and diffuse distribution of CO from the WRF model compared to that of GDAS. The GDAS ending locations remain concentrated near the area of release over the Strait (compared to the WRF locations). WRF-derived horizontal winds exhibit more detail than those from the coarser GDAS data. Vertical motions from WRF also are stronger than those from GDAS. These two factors lead to a greater dispersion of CO from WRF throughout the domain.

3.2.1 April

The WRF-derived CO trajectories are described first (Figs. 15a, c, e). April is the only study month with persistent low-level convergence within the Strait (Fig. 11a). Therefore, it is the only month with CO concentrations > 1 pptv within the Strait after 120 h. April exhibits three preferred trajectory paths (Fig. 15a): 1) north through the Strait into the Bay of Bengal, where CO heads west or east (red arrows), 2) directly west over Sumatra where CO bends to the southwest and moves toward the southern Indian Ocean (green arrow), and 3) east over the Malay Peninsula where CO spreads out over the South China Sea (blue arrow). The majority of CO from the Strait during April remains near the Strait and Bay of Bengal, yielding the large CO concentrations between the Equator and 10° N and 85° and 100° E (Fig. 15a). The winds producing these trajectories are primarily below 5 km, and are part of the low-level, counterclockwise flow off the northwest coast of Sumatra (Fig. 11a).

Those trajectories that do not encounter this low-level flow are transported north. Westerly winds above 8 km (Fig. 13a) greatly influence the trajectories north of 10° N, producing a maximum of CO between 10 and 16 km (Fig. 15c). They extend from the maximum in the Bay of Bengal to the western Pacific between Taiwan and the northern Philippines—nearly 20° longitude east from the Strait (red arrow), and are a result of the large, upper-level anticyclonic flow over the western Pacific (Fig. 13a). The CO that extends from the Strait into the Bay of Bengal near the surface does not penetrate far inland and is mostly confined to the coasts of eastern Sumatra, northwest Malay Peninsula, and southwest Thailand. The maximum CO over Sumatra occurs near the location of the daytime lightning maximum in Fig. 5; a location of local convergence. The concentrations over land occur mostly on the Strait-side of the mountains on each respective landmass (Fig. 15e). CO spreads out through the South China Sea primarily below 6 km to the coast of Borneo (blue arrow).

Latitudinal and longitudinal cross sections show that CO calculated in 1 km layers reaches altitudes greater than 20 km (Figs. 15c, e). The height of the tropopause at this time is ∼16–17 km altitude. Greatest concentrations in the UTLS are at ∼16–18 km between ∼3° S and 5° N (Fig. 15c) and ∼88° and 95° E (Fig. 15e). Paths of the CO trajectories (not shown) indicate that this maximum is caused by a constant pumping of CO to the UTLS by the widespread convection. The primary CO outflow layer is at altitudes between 6 and 12 km, with a maximum at 8 km. This upper-level dispersion can be seen in the spread of CO concentrations between 10 and 16 km mostly to the north (Fig. 15c) and east (Fig. 15e). CO is abruptly diverted north or south near 80° E (Figs. 15a, c) due to the collision of easterly flow meeting westerly flow from Africa (Fig. 13a). Low-level CO disperses from the equator to ∼10° N (Fig. 15c). Longitudinally, there is a maximum near 91° E and the Strait (Fig. 15a). CO below ∼2 km disperses throughout the South China Sea to ∼110° E. The dispersion is primarily a result of the low-level flow, which contains little-to-no deep convection. The low-level trajectories over the eastern Indian Ocean are a result of non-convective upslope and downslope flow moving up, over, and down the Barisan Mountains on Sumatra, coupled with CO that is bent around the northern tip of Sumatra in the wake of the wind off the northwest coast.

Trajectories and CO concentrations from the GDAS data (Figs. 15b, d, f) are most dissimilar to those from WRF during April when the GDAS CO field is the least horizontally displaced (Figs. 15a, b). The three primary ending maxima are 1) a path from the Strait to the Bay of Bengal (red arrow), 2) a pattern west over Sumatra that arcs to the southwest (green arrow), and 3) over the South China Sea (blue arrow), similar to the WRF trajectories. The two primary differences with WRF are the arc from the Bay of Bengal to the northern Philippines (top right red arrow Fig. 15a); and that the maximum ending locations cover most of Peninsular Malaysia, the central to southern Strait, and Sumatra along the equator. These latter patterns are mostly non-existent in the WRF trajectories.

Unlike WRF-derived CO, little GDAS-derived CO during April reaches altitudes of 10 km (Figs. 15d, f), with most terminating below 4 km at 120 h. This occurs because the coarse-resolution GDAS data does not adequately simulate the strong vertical motions associated with deep convection. Vertical motions (Fig. 14) are too weak to transport many particles to the upper levels within 120 h. WRF vertical motions are $\sim$3.5 km h^{-1} in the convective cores, whereas those from GDAS are $\sim$0.22 km h^{-1}. The maximum at 6–8 km (Fig. 15d) is due to convection over the Barisan Mountains.

3.2.2 October

The WRF-derived CO trajectories from the Strait during October mostly extend westward and disperse throughout the Indian Ocean after 120 h (Fig. 16). This occurs because of the prevalent easterlies throughout the study domain above 2 km (Figs. 12c,

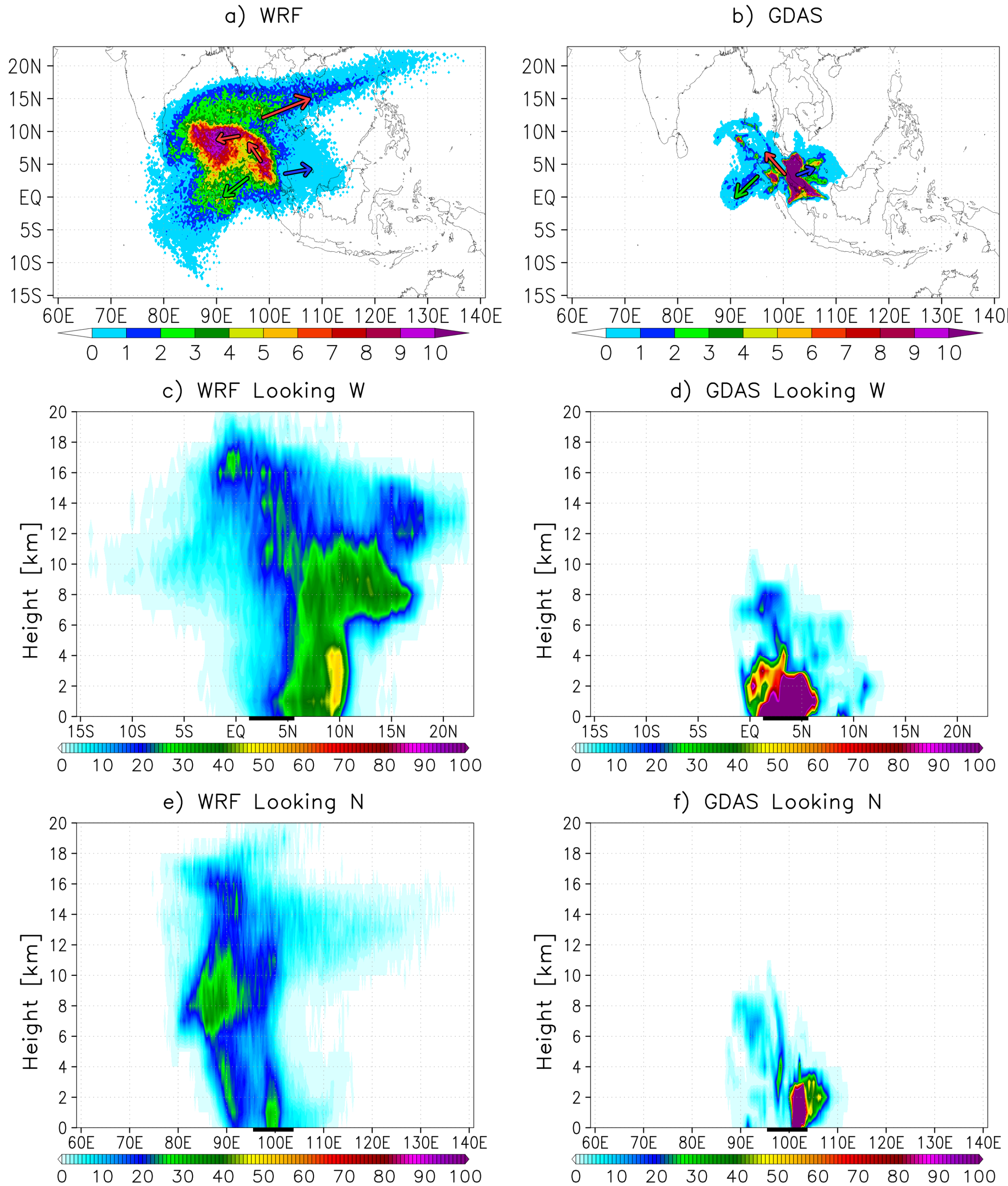

FIG. 15. April WRF (left column) and GDAS (right column) HYSPLIT results. Concentrations of proxy CO particles are shown in pptv on a 0.25° × 0.25° × 1 km grid. Horizontal plots (a) and (b) are columnar sums from the surface to the model top, latitudinal cross sections (c and d) are domain sums that include all longitudes, and the longitudinal cross sections (e and f) include all latitudes. The black line below the plots between 1° and 6° N in (c) and (d) and 95° and 102° E in (e) and (f) is the approximate location of the Strait.

13c). The low-level CO from the Strait that heads west is forced up and over the Barisan Mountains where it encounters mid-level easterly flow. CO concentrations are maximized over the eastern Indian Ocean between 5° S and 5° N, with a secondary maximum between 65° and 72° E and 5° and 9° N (Fig. 16a). CO that experiences deep convection within the Strait moves south over the western regions of the domain (Fig. 16c) due to the northerly flow at heights of 8–15 km (Fig. 13c) in the southern Indian Ocean. Some CO disperses throughout the Maritime Continent over the eastern and southern edges of the domain. This is the result of deep convection within the Strait where CO reaches altitudes greater than 18 km (Figs. 16c, e). Trajectory paths (not shown) reveal that some CO passes over the South China Sea, but then disperse so greatly that at 120 h the region is relatively void of CO from the Strait. To summarize, the primary path is west over Sumatra and then over the Indian Ocean. The few trajectories that remain in the Strait region are limited to the western coasts of the Malay Peninsula, the Strait, and through northern Sumatra.

The cross sections of CO concentrations (Figs. 16c, e) reveal the impact of the strong mid-to-upper level winds discussed previously (Figs. 12c, 13c). CO reaches altitudes greater than 18 km, but with smaller concentrations above 14 km than during April (Fig. 15). Similar to April, the height of the tropopause is ~16–17 km altitude. The trajectories slant longitudinally (Fig. 16e) from the surface of the eastern Indian Ocean (~90° to 95° E) to the edge of the domain at 60° E in the upper troposphere. The maximum outflow is at ~11–15 km. The constant pumping of CO from deep convection, coupled with strong mid-to-upper-level flow, results in the rapid westward transport to create this slanted configuration. The majority of the low-level CO travels north where it is caught in the wake on the northwestern coast of Sumatra. This transport is similar to that during April, but occurs at a faster rate, resulting in a clearing of the Strait. This is displayed by the large concentration off the northwest coast of Sumatra (Fig. 16a), in Fig. 16c where substantial surface concentrations are between 1° and 5° N, and in Fig. 16e where there is a relatively dense concentration between the surface and ~4 km and 91° to 95° E. The large maximum over the eastern Indian Ocean (Fig. 16a) is a result of the constant deep convective pumping of CO within the Strait and orographic lifting over the mountains. The CO near 12 km altitude is primarily caused by convection in the Strait, whereas the CO near ~4–8 km is primarily orographically forced. Overall, CO is better dispersed out of the Strait during October than April (Figs. 16a, c, e).

GDAS-derived CO trajectories during October (Figs. 16b, d, f) exhibit some horizontal and vertical similarities to those from WRF, but with much less dispersion. Although horizontal wind speeds from GDAS (Figs. 11, 12, 13) are similar to those from WRF, and similar to those during April, GDAS's relatively weak convective vertical motions (Fig. 14) do not produce sufficient vertical transport. Specifically, WRF-derived vertical motions in convective cores are ~2.5 km h^{-1}, whereas GDAS-derived vertical motions are ~0.25 km h^{-1} at their peak intensity. Unlike WRF, the maximum CO concentration is within the Strait and on the western coast of the Malay Peninsula (Fig. 16b). A maximum also extends from near central Sumatra to just off its western coast, and is at altitudes < 8 km (Fig. 16f). This is a result of the topography of the Barisan Mountains. This CO does not extend high enough to encounter the strong easterly flow of the upper-levels (Fig. 13d) because of weaker orographic convection, and therefore remains closely concentrated near the Strait.

3.2.3 February

The WRF-derived CO trajectories from the Strait during February exhibit the most intriguing pattern of all three months with a slanted ε shape (Fig. 17). This highlights the transitional flow described earlier. The trajectories display three distinct ending locations: 1) an arc extending from the western coast of Sumatra into the Bay of Bengal and then toward

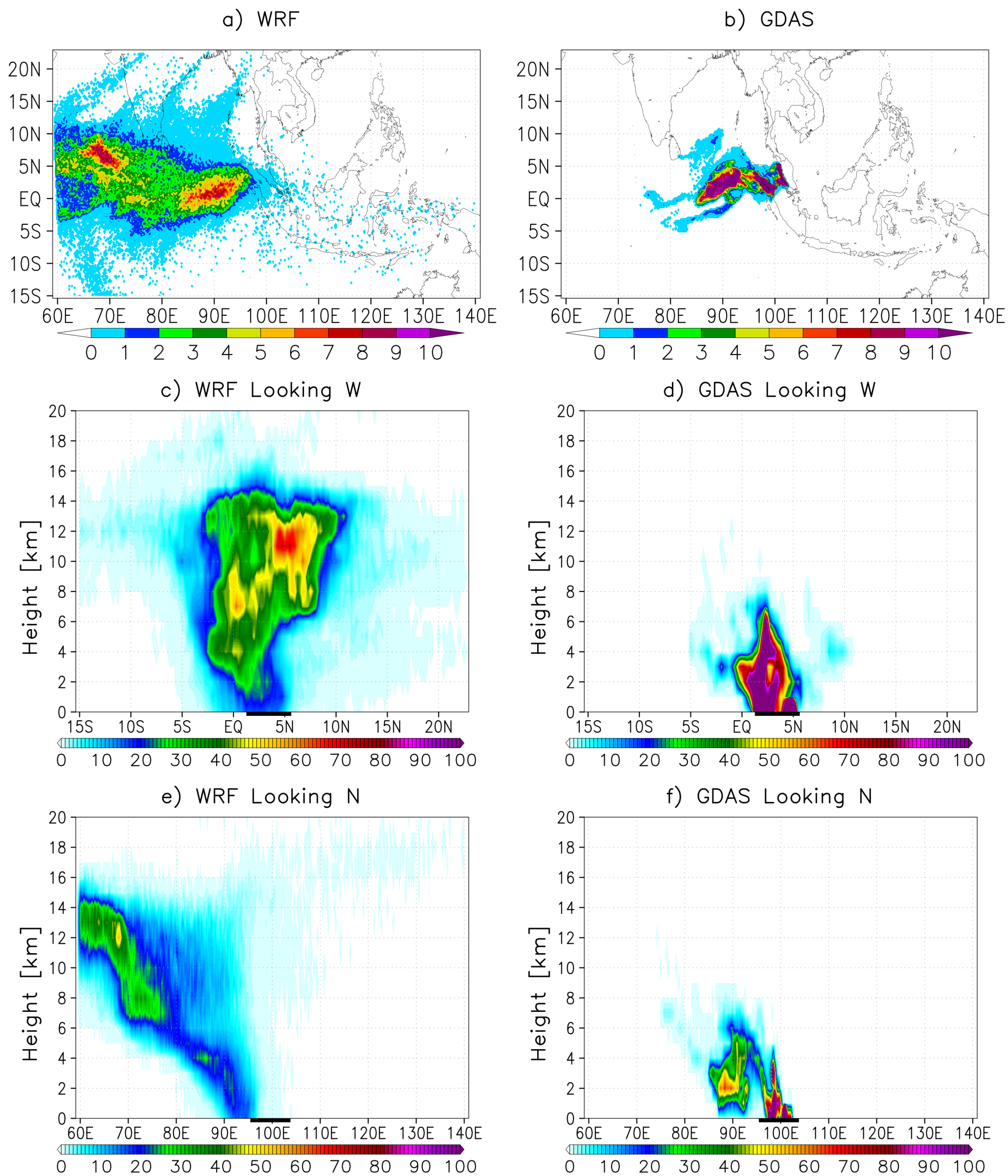

FIG. 16. As in Fig. 15, but for October.

the northern Philippines (red arrows), 2) the Indian Ocean near the equator, between 70° and 100° E (green arrow), and 3) a path extending from the western coast of Sumatra, over Java, and through the southern regions of the Maritime continent and northern Australia (blue arrows). The preferred paths of the trajectories are similar to their ending locations (shown by the arrows). Contrary to April and October, the height of the tropopause is lower, at ∼15–16 km altitude. The CO that exits in the Strait over northern Sumatra either moves north to the Bay of Bengal or west toward the Indian Ocean (Fig. 17a) at altitudes of ∼10–16 km (Fig. 17c) and ∼6–14 km (Fig. 17e), respectively (red arrows). The southern-moving trajectories follow the Barisan Mountains and western coasts of Sumatra toward Java and Australia, and are primarily below 5 km (blue arrows). CO that experiences deep convection is at altitudes of 10–16 km in this region (Figs. 17c, e). The ending locations of the westward-moving CO are similar to those during October (Fig. 16), being influenced by the dominant mid-to-upper level easterly winds (Figs. 12e, 13e). However, a branch flows toward the Bay of Bengal similar to April (Fig. 15a). The farthest west CO concentrations, ending at altitudes exceeding 6 km (Fig. 17e), are topographically forced and associated with the mid- to upper-level easterly flow (Figs. 12e, 13e). The southwestern region of the Maritime Continent is influenced by air from the Strait, whereas the South China Sea is relatively unaffected. This is due to the fast, low-level, northeasterly flow over the South China Sea (Fig. 11e), which inhibits eastward low-level movement. A small concentration of CO remains in the Strait. Some of this remaining CO moves south over Sumatra where it combines with the CO spreading toward Australia (blue arrows). These trajectories are greatly influenced by the aforementioned northeasterly flow from the South China Sea and strong northwesterly flow over the eastern Indian Ocean.

The ending altitudes of the February CO trajectories are similar to those during April (Fig. 15) and October (Fig. 16), but exhibit much sparser CO concentrations in the upper-troposphere (Figs. 17c, e). Outflow from the deep convection is evident at ~5–8 and ~9–12 km, with another maximum, not related to deep convection, located primarily below 2 km. The longitudinal cross section during February (Fig. 17e) slightly resembles that of October (Fig. 16e), with a westerly-slanting orientation from ~4 km at 85° E to ~7 km at the edge of the domain (which is considerably lower in the troposphere than October). This similarity is a result of the two months having relatively similar mid-level winds (Figs. 12c, e). The distinguishing characteristic of February's trajectories is its large low-level CO concentrations. Unlike any other month, the low-level CO reaches the northern and southern extents of the domain, and is farthest east (Fig. 17a). The counterclockwise flow near Borneo, and the strong low-level jet southeast of Sumatra (Fig. 11e) greatly influence the eastward-moving CO. The two low-level maxima at ~89° E and ~96° E, result from westward propagation of CO over the Barisan Mountains.

The February CO trajectories derived from the GDAS data (Figs. 17b, d, f) arc northward from the western coast of Sumatra to the Bay of Bengal and down to the northern tip of Australia (Fig. 17b), similar to the WRF-derived trajectories. A barely distinguishable westward-moving CO signal is apparent over the Indian Ocean. The maximum in the WRF-derived CO over the eastern Indian Ocean is shifted to central to southern Sumatra, with maxima over the northeastern Indian Ocean. This is due to the stronger, low-level, WRF-derived winds over the South China Sea (Fig. 11e) having more influence than the GDAS-derived winds (Fig. 11f). The WRF model winds transports CO farther west over Sumatra than do the GDAS winds. Since large-scale winds above the PBL in the outer domain are nudged to analyses for the WRF simulations, this extra displacement must be from the low-level mesoscale circulations over Sumatra. Contrary to WRF, a CO maximum is found within the Strait.

The low-level dispersion during February (Figs. 17d, f) is similar to the WRF trajectories, but with most of the dispersion below 4 km instead of 2 km. This is primarily due to CO spreading south and north along the Barisan Mountains. The maximum at ∼9–11 km centered at the Equator is due to orographic convection. Similar to April and October, the parameterized GDAS convection produces vertical motion that is much weaker than from WRF. This inhibits ascent to the mid and upper levels. WRF-derived vertical motions are $\sim$2.8 km h^{-1} at their peak intensity within convective cores, whereas GDAS-derived vertical motions are $\sim$0.18 km h^{-1}. The convective core within the WRF model is thinner and lower in the atmosphere than April and October, and the GDAS core is inconsistent in strength in the vertical. Overall both models' vertical motions are weaker during February than during April or October. This is consistent with the instability (Fig. 7), and amount of lightning (Fig. 4) during these months.

3.3 Vertical concentration and fluxes

Figure 18 shows the vertical profile of CO concentration (in pptv) for each study period and model. The concentrations were summed over the entire domain at 1 km vertical intervals from the surface to 20 km. The GDAS-derived CO trajectories (dashed lines) are mostly concentrated in the lower troposphere, whereas the WRF-derived trajectories are more evenly distributed throughout the depth of the model domain. Focusing first on the WRF distributions, February has the greatest low- and mid-level concentrations ($<$ 8 km); October has the most mid-to-upper-level concentrations (8–14 km); and April has the greatest upper-level concentrations ($>$ 14 km). These results are consistent with the results in Figs. 4, 7, and 14. April has the greatest CAPE (Fig. 7), greatest amount of lightning (Fig. 4), and the strongest upward vertical motions within convective cores (Fig. 14). October is the second-most unstable month, the second greatest lightning producer, and has the second

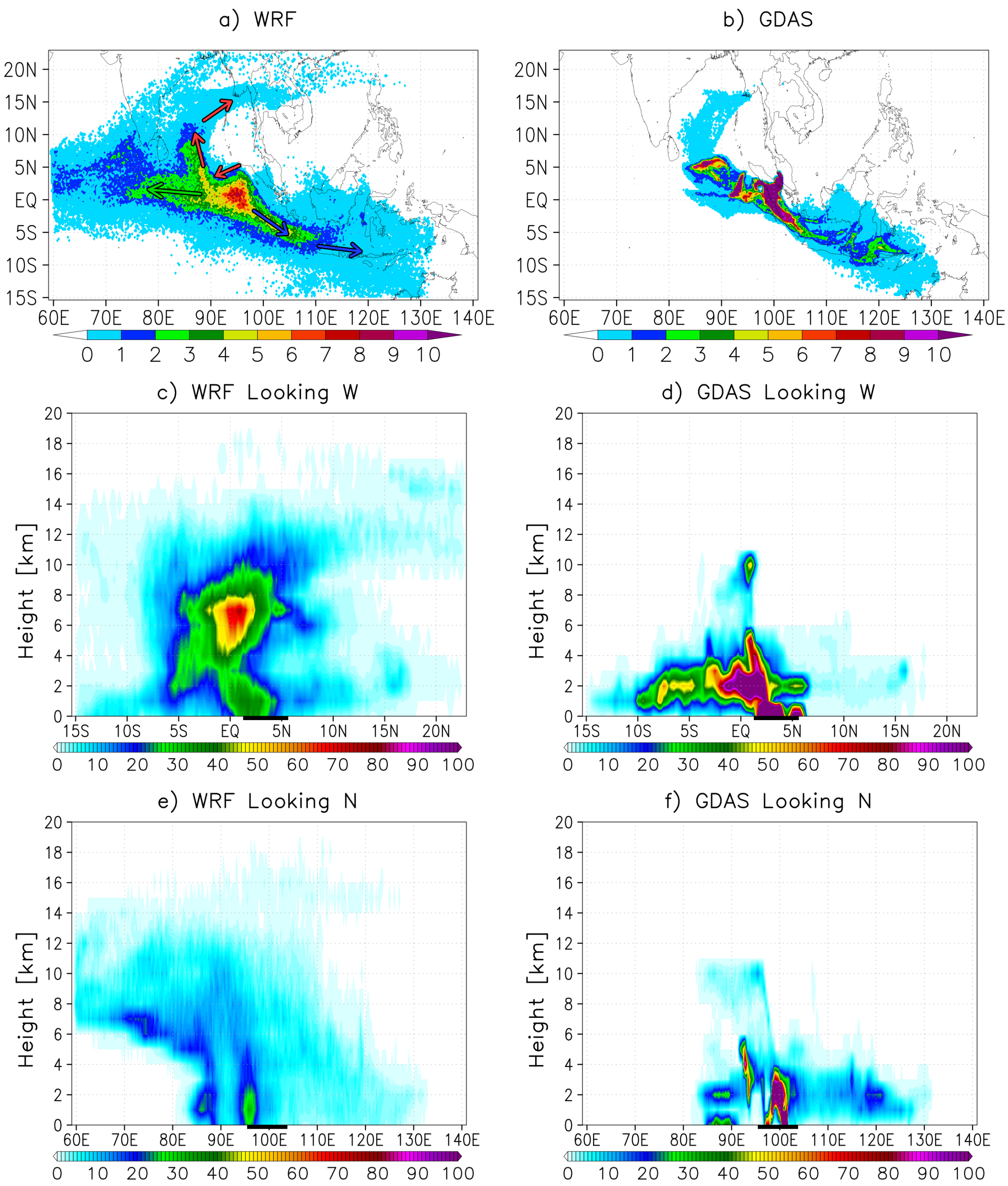

FIG. 17. As in Figs. 15 and 16, but for February.

strongest deep convective vertical motions (above 7 km). Therefore, some of its CO reaches the UTLS, but in smaller numbers than during April. February is the most convectively stable of the three months studied, with the least amount of lightning. Therefore, the greatest concentration of CO from the Strait is in the mid-to-lower troposphere. These results are opposite those from GDAS—the low-level maximum concentration is variable between months. February has the greatest concentration at ~9–10 km. This is counter-intuitive to Figs. 4, 7, and 14 since greater instability (CAPE) should result in deeper convection, and therefore greater CO concentrations in the upper troposphere. This highlights the inadequacies of the GDAS data to accurately simulate deep convection, since April and October should have the greatest concentrations in the mid-to-upper troposphere.

Figure 19a displays the vertical mass flux of CO from the Strait for the entire domain at 1 km vertical intervals. Vertical flux for the Strait alone will be described later in Fig. 19b. Every HYSPLIT particle was followed for the 120 h duration of its integration, and each time one passed through a level, the level was counted. Results show that the net CO mass flux is positive (upward) during each month. This means that the domain, as a whole, is efficient at transporting CO vertically due to the large amount of deep convection. Focusing on the WRF results, April exhibits the most upward, low-level CO mass flux ($<$ 3 km); October marginally has the greatest at ~3–8 km; and April again has the strongest upward flux $>$ 8 km. Conversely, April has the greatest downward CO mass flux $<$ 2 km, February has the greatest at ~3–7 km, and April has the greatest $>$ 7 km. Concerning the net vertical CO mass flux, October has the greatest net flux from 1 to 12 km, and April is the largest otherwise. The GDAS results show that the majority of its vertical movement happens below 6 km. Even with these less-desirable results, April still has the largest positive net flux higher in the troposphere than any other month (which in this case is ~6 km, as compared to the $>$ 12 km from the WRF trajectories).

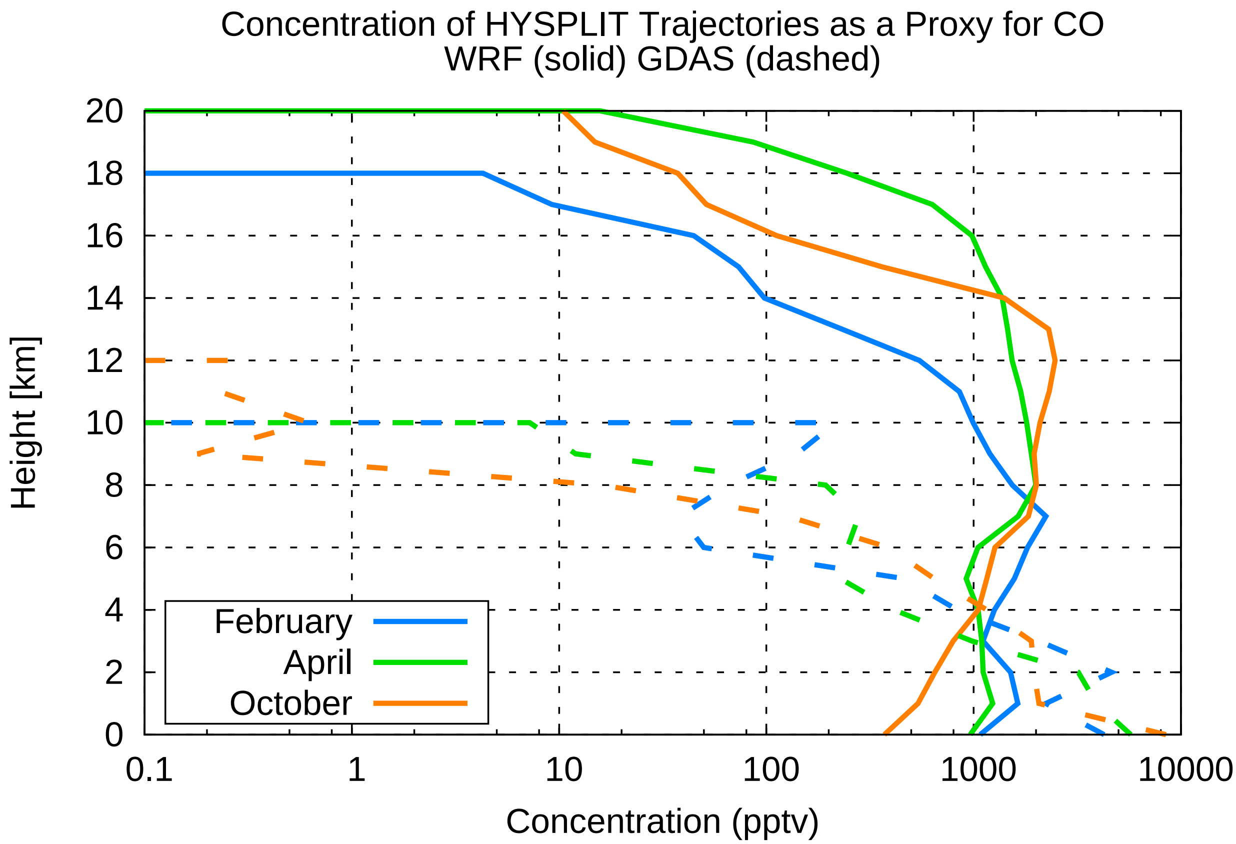

FIG. 18. Vertical profiles of concentrations of HYSPLIT trajectories as a proxy for CO (pptv) at various levels from WRF (solid) and GDAS (dashed). Vertical grid spacing is 1 km.

Figure 19b shows the vertical mass flux of CO from the Strait that occurs solely over the Strait. The same technique as in Fig. 19a was used to calculate mass flux, but only if the particle's displacement was within the confines of the Strait (described in Fig. 4), whereas Fig. 19a considers the total extent of d01. When a HYSPLIT particle leaves the Strait and does not return, it is no longer counted. Because of this technique, there is a smaller mass flux in Fig. 19b compared to that of Fig. 19a.

The CO fluxes from WRF and GDAS in the low levels (< 2 km) are somewhat comparable (Fig. 19b), but the values then diverge with increasing altitude as the ability of the WRF model to better simulate deep convection becomes evident. October has the greatest WRF-derived positive and net flux from the surface to ~11 and 13 km, respectively. Above these altitudes, April has the greatest mass flux. Conversely, for the entire-domain (Fig. 19a), April has the smallest WRF-derived net flux from the surface to ~9 km. The profiles of vertical flux generally are similar to those of vertical motion (Fig. 14). The exception is the GDAS data where the maximum upward motion is located at > 6 km, while the maximum mass flux is at < 6 km. The overall results are consistent with those of Figs. 4 and 7 where the two most unstable months and greatest lightning producing months (of the three studied) exhibit the greatest net flux. April, being the greatest lightning producer and most unstable, has the largest net flux in the upper troposphere.

Klich and Fuelberg (2013) studied the impacts of model resolution on the vertical transport of CO during the passage of a mid-latitude wave cyclone and associated squall line in Asia. Their Fig. 15 compares vertical CO fluxes from the various model resolutions used in WRF-Chem. The vertical flux profiles shown in Fig. 19 of this study are similar to those in Klich and Fuelberg (2013), with both exhibiting bell-shaped profiles. However, the mass fluxes described in Klich and Fuelberg (2013) are considerably greater than those presented here. Their study area was located in coastal China, an area with much greater surface CO. Their simulations also considered all sources of CO, whereas this study limited the CO source to non-road traffic (described earlier) within the Strait—a considerably smaller contribution. The sources in Southeast Asia provided > 200 ppbv (parts per billion by volume) of CO, whereas in the Strait, non-road transportation provided ~6 pptv of CO (using an approximate area of 58.9×10^3 km^2, a depth of 500 m, an average pressure of 966 hPa, an average temperature of 298 K, a molecular mass of air of 28.97 g mol^{-1}, and the Ideal Gas Law to get the ratio of CO to air). The major difference between their study and this study is that the Strait is a virtually constant source of ship pollution and deep convection, causing a relatively persistent vertical transport of pollutants. In the China case of Klich and Fuelberg (2013), the extreme buildup of low-level pollution was rapidly exported by the deep convection and then gradually increased after the convection had moved eastward.

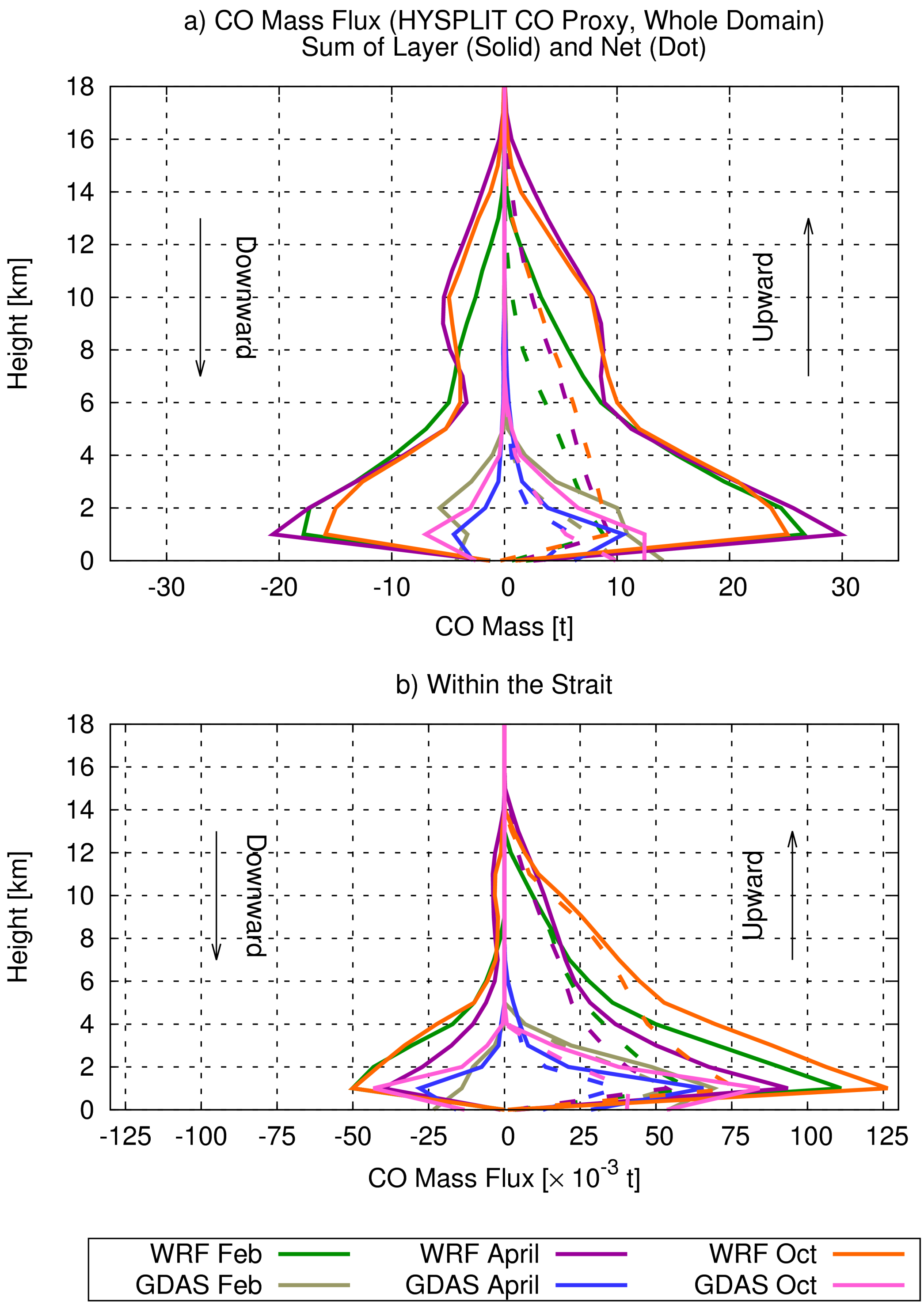

FIG. 19. CO mass flux for each study period calculated a) over the entire domain and b) only within the Strait. Sums within 1 km layers (solid) and net values (dashed).

CHAPTER 4

SUMMARY AND CONCLUSIONS

Ships account for more than 11, 4, and 2% of global anthropogenic emissions of NO_x, SO_2, and CO_2, respectively. The Strait of Malacca is a region of intense maritime traffic, and previous research and satellite observations (Fig. 2) have shown it to be a local maximum of ship emissions. Additionally, the Strait is a region of frequent and widespread deep convection, as evidenced by WWLLN lightning observations. The climatological distribution of lightning observations within the Strait (Fig. 4) exhibits a bimodal annual distribution with maxima during April and October. These maxima are out of phase with the Asian monsoon and are linked to the passage of the ITCZ. Although climatological precipitation data for the Strait have shown October to be the wettest month, April contains the most lightning, and is therefore the most convective of the two. February exhibits the least amount of lightning within the Strait. The WWLLN observations also reveal that the Strait has a diurnal lightning distribution, with a nighttime (1900–0700 LT) lightning maximum that is greater than its daytime (0700–1900 LT) counterpart over the surrounding landmasses (Fig. 5).

Previous studies of ship emissions have used coarse-resolution global models. However, regional-scale models are necessary to adequately resolve the convection in geographically complex regions such as the Strait. Global models, with coarse resolution, do not provide the necessary detail to depict the intricate mesoscale forcing mechanisms in the region. These mechanisms include sea/land breezes, katabatic/anabatic winds, and cold-air outflows from previous convection (Fig. 10). If these features are inadequately resolved, deep convection can be inaccurately simulated, along with the subsequent transport of pollutants.

This study used the high-resolution WRF model at 2 km grid spacing with explicitly resolved convection. WRF was run from 1200 UTC on the 13th day through 0000 UTC on the 21st day (180 h run) of February, April and October, with the first 12 h of each run considered as model spin-up and not used. April and October were chosen since they are the months with the most deep convection (i.e., lightning). Conversely, February was chosen because of its small amount of lightning.

HYSPLIT was used to simulate the transport of three thousand, randomly placed (x, y, z) particles representing CO ship emissions. Their initial locations were bound horizontally by the coasts of the Strait (defined in Fig. 4) and vertically by 500 m. Forward trajectories of the HYSPLIT particles were calculated between 0000 UTC on the 14th day to 0000 UTC on the 21st day of each study month. They were released every hour for the first 48 h and terminated at 120 h. The particles were a proxy for CO which has a long residence time and does not readily chemically react with other molecules. Using EDGAR v4.2 emissions, with the "non-road transportation" sub-dataset, a mass was assigned to each HYSPLIT particle, which allowed the calculation of atmospheric concentrations of CO at locations in three dimensional space. We assumed that all non-road EDGAR CO emissions were from ships, although this certainly is not the case. However, the visible correlation between EDGAR emissions (not shown) to GOME-2 observations (Fig. 2) and easily-identifiable shipping lanes provides support for this assumption.

The ending locations of the trajectories (CO particles) were summed and binned on a $0.25° \times 0.25° \times 1$ km grid to reveal the horizontal and vertical transport each month. WRF-derived trajectories during the highly convective month of April (Fig. 15) reached higher altitudes (Fig. 18) than those during October (Fig. 16) and February (Fig. 17). Table 2 subdivides the entire study domain into three vertical layers (lower, middle-to-upper, and UTLS), and displays an aerial sum of CO concentrations at each layer. February produces the greatest ending transport in the lower troposphere (0–7 km); October exhibits the greatest in the middle-to-upper troposphere (8–14 km); and April exhibits the most in the UTLS (15–21 km). Thus, April and October are the best transporters of CO to high altitudes. This is consistent with the lightning observations (Fig. 4) and CAPE climatology (Fig. 7), which show April as the most lightning prolific month, October as the second greatest, and February as the least of the three.

HYSPLIT results from WRF simulations (2 km horizontal grid spacing) are considerably different from those using GDAS data provided by the ARL (110 km grid spacing; Table 2). GDAS-derived CO concentrations in the lower-troposphere are greater than those from WRF each month. February has the largest GDAS-derived concentrations in the mid-to-upper troposphere; April is the second greatest; and October is third. Unlike results from WRF, none of the three months exhibit any CO concentration from the Strait in the UTLS when GDAS data are used.

TABLE 2. Summary of HYSPLIT particle locations after 120 h (CO proxy concentrations; pptv) summed over three layers within the entire domain for WRF [GDAS] for each of the three months of study.

	February	**April**	**October**
15–21 km	131 [0]	3098 [0]	591 [0]
8–14 km	5459 [421]	11746 [212]	14547 [17]
0–7 km	12208 [14571]	9062 [14990]	7669 [16709]

CO reaching higher altitudes can experience long-range transport since wind speeds generally increase with altitude (Figs. 11–13). Thus, the more intense the convection, the more likely there is long range transport. WRF-derived October trajectories display this characteristic well, with an immediate westward transport of CO after release. April has the weakest winds of the three months, causing the trajectories to be less horizontally diffuse. The WRF-derived horizontal and vertical winds are more detailed than those from the coarser GDAS data. The higher resolution vertical motions also are stronger. These two factors produce a greater dispersion of WRF trajectories and their CO throughout the domain. Conversely, the GDAS trajectories are more horizontally concentrated than those from WRF.

Horizontal patterns of CO generally are similar between the two models, but those from WRF trajectories are weaker and more diffuse. April ending trajectory locations primarily are north of the Strait (where they bend west or east), directly west of the Strait into the Indian Ocean, or east over the Malay Peninsula where they diffuse over the South China Sea (Fig. 15). October trajectories exhibit the most long-range CO transport with a long, extended signal west to the edge of the domain (Fig. 16). February exhibits the most low-level diffusion where particles primarily move west over the Indian Ocean or South along Sumatra where they end near northern Australia (Fig. 17). The greater GDAS-derived CO concentrations near the Strait are a testament to the poor dispersion due to coarse-resolution meteorological data.

CO reaches altitudes greater than 18 km when using the WRF meteorological input due to its more intense simulated deep convection within the Strait. Similarly, WRF's finer horizontal resolution resolves the earlier-mentioned mesoscale circulations that provide the low-level convergence needed for convective initiation, and the subsequent transfer of CO out of the Strait. Conversely, the GDAS meteorological input produces trajectories that are mostly concentrated near the surface below 6 km. The GDAS data does not have sufficient deep convection within the Strait to yield the same vertical transport as the WRF model.

Outflow regions from WRF are primarily above 8 km. The GDAS-derived outflow regions (if present) occur primarily below 6 km and are not as defined as those from WRF.

Vertical fluxes of CO (Fig. 19) were calculated to quantify the vertical transport of ship emissions. WRF, rather than GDAS, showed the greatest values of upward and downward vertical flux over the whole domain and within the Strait itself. Over the entire domain and within the Strait, April has the greatest upward flux above 8 and 11 km, respectively. This is consistent with the lightning observations. The GDAS results showed that vertical flux ceases around 6 km altitude. This displays the inability of coarse-resolution models to simulate the transport of particles in deep convection. Results from this study compare well with those from Klich and Fuelberg (2013).

This study has shown that deep convection can horizontally and vertically transport ship emissions within the Strait of Malacca to distant locations. It also has shown that the limitations of coarse-resolution models to simulate deep convection can have dramatic impacts on pollution transport. Higher-resolution models are needed to accurately simulate the fine-scale details of convection within geographically complex regions such as the Strait. Katabatic/anabatic winds, sea/land breezes, and cold-air outflows associated with the deep convection found within the Strait must be faithfully resolved to adequately model the transport of ship pollutants. Constant pumping of surface air to the mid-to-upper troposphere/lower stratosphere from the diurnal cycle of deep convection over and within the Strait allows for continuous polluting of the mid-to-upper troposphere/lower stratosphere. Unlike a squall line event (such as the one studied in Klich and Fuelberg 2013), the Strait provides a constant source of pollutants above the surface on a daily time scale.

Potential improvements to this study would be to compare the transport of emissions using high-resolution WRF with chemistry (WRF-Chem) simulations and GCTMs (such as those mentioned in Chapter 1). Isolating ship emissions from an emissions dataset, coupled with a high-resolution chemistry model, would further reveal the impact of ships on the atmosphere. The study of complex ship emissions such as NO_x and SO_2 is needed. These two compounds are subject to dry and wet deposition and can drastically modify the environment where they deposit. High-resolution chemical modeling including these two species could build on the work of Streets et al. (1997) and Streets et al. (2000) to better estimate the contribution of ship emissions in Southeast Asia and the world.

REFERENCES

AAPA, cited 2013: World Port Rankings - 2011. [Available online at http://aapa.files.cms-plus.com/PDFs/WORLD%20PORT%20RANKINGS%202011.pdf].

Aldrian, E., L. Dümenil Gates, and F. H. Widodo, 2007: Seasonal variability of Indonesian rainfall in ECHAM4 simulations and in the reanalyses: The role of ENSO. *Theor. Appl. Climatol.*, **87**, 41–59, doi:10.1007/s00704-006-0218-8.

Aldrian, E. and R. Dwi Susanto, 2003: Identification of three dominant rainfall regions within Indonesia and their relationship to sea surface temperature. *Int. J. Clim.*, **23**, 1435–1452, doi:10.1002/joc.950.

Aligo, E. A., W. A. Gallus, and M. Segal, 2009: On the Impact of WRF Model Vertical Grid Resolution on Midwest Summer Rainfall Forecasts. *Wea. Forecasting*, **24**, 575, doi:10.1175/2008WAF2007101.1.

Arritt, R. W., 1989: Numerical modelling of the offshore extent of sea breezes. *Quart. J. Roy. Meteorol. Soc.*, **115**, 547–570, doi:10.1002/qj.49711548707.

Arritt, R. W., 1993: Effects of the large-scale flow on characteristic features of the sea breeze. *J. Appl. Meteorol.*, **32**, 116–125, doi:10.1175/1520-0450(1993)032⟨0116:EOTLSF⟩2.0.CO;2.

Beirle, S., U. Platt, R. von Glasow, M. Wenig, and T. Wagner, 2004: Estimate of nitrogen oxide emissions from shipping by satellite remote sensing. *Geophys. Res. Lett.*, **31**, L18102, doi:10.1029/2004GL020312.

Berry, G. and M. Reeder, 2013: Objective identification of the intertropical convergence zone: Climatology and trends from the ERA-Interim reanalysis. *J. Clim.*, doi:doi:10.1175/JCLI-D-13-00339.1,inpress.

Boccippio, D. J., S. J. Goodman, and S. Heckman, 2000: Regional differences in tropical lightning distributions. *J. Appl. Meteorol.*, **39**, 2231–2248, doi:10.1175/1520-0450(2001)040⟨2231:RDITLD⟩2.0.CO;2.

Bovensmann, H., J. P. Burrows, M. Buchwitz, J. Frerick, S. Noël, V. V. Rozanov, K. V. Chance, and A. P. H. Goede, 1999: SCIAMACHY: Mission objectives and measurement modes. *J. Atmos. Sci.*, **56**, 127–150, doi:10.1175/1520-0469(1999)056⟨0127:SMOAMM⟩2.0.CO;2.

Burrows, J. P., E. Hölzle, A. P. H. Goede, H. Visser, and W. Fricke, 1995: SCIAMACHY—scanning imaging absorption spectrometer for atmospheric chartography. *Acta Astronaut.*, **35**, 445–451, doi:10.1016/0094-5765(94)00278-T.

Burrows, J. P., et al., 1999: The Global Ozone Monitoring Experiment (GOME): Mission concept and first scientific results. *J. Atmos. Sci.*, **56**, 151–175, doi:10.1175/1520-0469(1999)056⟨0151:TGOMEG⟩2.0.CO;2.

Callies, J., E. Corpaccioli, M. Eisinger, A. Hahne, and A. Lefebvre, 2000: GOME-2-MetOP's second-generation sensor for operational ozone monitoring. *ESA Bull.*, **102**, 28–36.

Capaldo, K., J. J. Corbett, P. Kasibhatla, P. Fischbeck, and S. N. Pandis, 1999: Effects of ship emissions on sulphur cycling and radiative climate forcing over the ocean. *Nature*, **400**, 743–746, doi:10.1038/23438.

Chang, C. P., Z. Wang, J. Ju, and T. Li, 2004: On the relationship between western Maritime Continent monsoon rainfall and ENSO during northern winter. *J. Clim.*, **17**, 665–672, doi:10.1175/1520-0442(2004)017⟨0665:OTRBWM⟩2.0.CO;2.

Chang, C. P., Z. Wang, J. McBride, and C. H. Liu, 2005: Annual cycle of Southeast Asia—Maritime Continent rainfall and the asymmetric monsoon transition. *J. Clim.*, **18**, 287–301, doi:10.1175/JCLI-3257.1.

Chosson, F., R. Paoli, and B. Cuenot, 2008: Ship plume dispersion rates in convective boundary layers for chemistry models. *Atmos. Chem. Phys.*, **8**, 4841–4853.

Christian, H., K. Driscoll, S. Goodman, R. Blakeslee, D. Mach, and D. Buechler, 1996: The Optical Transient Detector (OTD). *Proceedings of the 10th International Conference on Atmospheric Electricity*, 10–14.

Christian, H., et al., 1999: The Lightning Imaging Sensor. *NASA conference publication*, NASA, 746–749.

Christian, H. J., et al., 2003: Global frequency and distribution of lightning as observed from space by the Optical Transient Detector. *J. Geophys. Res.: Atmos.*, **108**, 4005, doi:10.1029/2002JD002347.

Corbett, J. J., P. S. Fischbeck, and S. N. Pandis, 1999: Global nitrogen and sulfur inventories for oceangoing ships. *J. Geophys. Res.*, **104**, 3457–3470, doi:10.1029/1998JD100040.

Corbett, J. J. and H. W. Koehler, 2003: Updated emissions from ocean shipping. *J. Geophys. Res.: Atmos.*, **108**, 4650, doi:10.1029/2003JD003751.

Crowe, P. R., 1951: Wind and weather in the equatorial zone. *Trans. and Pap. (Inst. of Br. Geographers)*, **(17)**, pp. 23–76.

Dalsøren, S. B., M. S. Eide, Ø. Endresen, A. Mjelde, G. Gravir, and I. S. A. Isaksen, 2009: Update on emissions and environmental impacts from the international fleet of ships: The contribution from major ship types and ports. *Atmos. Chem. Phys.*, **9**, 2171–2194.

Davis, D. D., et al., 2001: Impact of ship emissions on marine boundary layer NO_x and SO_2 distributions over the Pacific Basin. *Geophys. Res. Lett.*, **28 (2)**, 235–238, doi: 10.1029/2000GL012013.

de Foy, B., M. Zavala, N. Bei, and L. T. Molina, 2009: Evaluation of WRF mesoscale simulations and particle trajectory analysis for the MILAGRO field campaign. *Atmos. Chem. Phys.*, **9**, 4419–4438.

Draxler, R. R. and G. D. Hess, 1997: Description of the HYSPLIT4 modeling system. NOAA Tech. Memo. ERL ARL–224, 25 pp.

Endresen, Ø., J. Bakke, E. Sørgård, T. Flatlandsmo Berglen, and P. Holmvang, 2005: Improved modelling of ship SO_2 emissions—a fuel-based approach. *Atmos. Environ.*, **39**, 3621–3628, doi:10.1016/j.atmosenv.2005.02.041.

Endresen, Ø., E. Sørgârd, J. K. Sundet, S. B. Dalsøren, I. S. A. Isaksen, T. F. Berglen, and G. Gravir, 2003: Emission from international sea transportation and environmental impact. *J. Geophys. Res.: Atmos.*, **108**, 4560, doi:10.1029/2002JD002898.

Estoque, M. A., 1962: The sea breeze as a function of the prevailing synoptic situation. *J. Atmos. Sci.*, **19**, 244–250, doi:10.1175/1520-0469(1962)019⟨0244:TSBAAF⟩2.0.CO;2.

Eyring, V., H. W. Koehler, J. van Aardenne, and A. Lauer, 2005: Emissions from international shipping: 1. The last 50 years. *J. Geophys. Res.: Atmos.*, **110**, D17305, doi:10.1029/2004JD005619.

Eyring, V., et al., 2010: Transport impacts on atmosphere and climate: Shipping. *Atmos. Environ.*, **44**, 4735–4771, doi:10.1016/j.atmosenv.2009.04.059.

Feng, J. and Y. L. Chen, 1998: Evolution of katabatic flow on the island of Hawaii on 10 August 1990. *Mon. Weather Rev.*, **126**, 2185, doi:10.1175/1520-0493(1998)126⟨2185:EOKFOT⟩2.0.CO;2.

Folkins, I. and R. V. Martin, 2005: The vertical structure of tropical convection and its impact on the budgets of water vapor and ozone. *J. Atmos. Sci.*, **62**, 1560–1573, doi: 10.1175/JAS3407.1.

Franke, K., A. Richter, H. Bovensmann, V. Eyring, P. Jöckel, P. Hoor, and J. P. Burrows, 2009: Ship emitted NO_2 in the Indian Ocean: Comparison of model results with satellite data. *Atmos. Chem. Phys.*, **9**, 7289–7301.

Fujita, M., F. Kimura, and M. Yoshizaki, 2010: Morning precipitation peak over the Strait of Malacca under a calm condition. *Mon. Weather Rev.*, **138**, 1474–1486, doi:10.1175/2009MWR3068.1.

Golding, B. W., 1993: A numerical investigation of tropical island thunderstorms. *Mon. Weather Rev.*, **121**, 1417, doi:10.1175/1520-0493(1993)121⟨1417:ANIOTI⟩2.0.CO;2.

Gray, W. M. and R. W. Jacobson, 1977: Diurnal variation of deep cumulus convection. *Mon. Weather Rev.*, **105**, 1171, doi:10.1175/1520-0493(1977)105⟨1171:DVODCC⟩2.0.CO;2.

Grell, G. A. and D. Dévényi, 2002: A generalized approach to parameterizing convection combining ensemble and data assimilation techniques. *Geophys. Res. Lett.*, **29**, 1693, doi:10.1029/2002GL015311.

Grooß, J. U. and J. M. Russell III, 2005: Technical note: A stratospheric climatology for O_3, H_2O, CH_4, NO_x, HCl and HF derived from HALOE measurements. *Atmos. Chem. Phys.*, **5**, 2797–2807.

Haglind, F., 2008: A review on the use of gas and steam turbine combined cycles as prime movers for large ships. Part III: Fuels and emissions. *Energy Convers. Manage.*, **49 (12)**, 3476 – 3482, doi:http://dx.doi.org/10.1016/j.enconman.2008.08.003.

Hales, J. M. and M. T. Dana, 1979: Precipitation scavenging of urban pollutants by convective storm systems. *J. Appl. Meteorol.*, **18**, 294–316, doi:10.1175/1520-0450(1979)018⟨0294:PSOUPB⟩2.0.CO;2.

Hamada, J. I., M. D. Yamanaka, J. Matsumoto, S. Fukao, P. A. Winarso, and T. Sribimawait, 2002: Spatial and temporal variations of the rainy season over Indonesia and their link to ENSO. *J. of the Meteorol. Soc. of Japan. Ser. II*, **80 (2)**, 285–310.

Hane, C. E., 1978: Scavenging of urban pollutants by thunderstorm rainfall: Numerical experimentation. *J. Appl. Meteorol.*, **17**, 699–710, doi:10.1175/1520-0450(1978)017⟨0699:SOUPBT⟩2.0.CO;2.

Hara, M., T. Yoshikane, H. G. Takahashi, F. Kimura, A. Noda, and T. Tokioka, 2009: Assessment of the diurnal cycle of precipitation over the Maritime Continent simulated by a 20 km mesh GCM using TRMM PR data. *J. of the Meteorol. Soc. of Japan. Ser. II*, **87A**, 413–424.

He, J., C. Sun, Y. Liu, J. Matsumoto, and W. Li, 2007: Seasonal transition features of large-scale moisture transport in the Asian-Australian monsoon region. *Adv. Atmos. Sci.*, **24**, 1–14, doi:10.1007/s00376-007-0001-5.

He, J., M. Wen, L. Wang, and H. Xu, 2006: Characteristics of the onset of the Asian summer monsoon and the importance of Asian-Australian "land bridge". *Adv. Atmos. Sci.*, **23**, 951–963, doi:10.1007/s00376-006-0951-z.

Heath, N. K. and H. E. Fuelberg, 2013: Using a WRF simulation to examine regions where convection impacts the Asian summer monsoon anticyclone. *Atmos. Chem. Phys. Discuss.*, **13**, 24 809–24 853, doi:10.5194/acpd-13-24809-2013.

Hendon, H. H. and K. Woodberry, 1993: The diurnal cycle of tropical convection. *J. Geophys. Res.*, **98**, 16 623–16 638, doi:10.1029/93JD00525.

Heymsfield, G. M., L. Tian, A. J. Heymsfield, L. Li, and S. Guimond, 2010: Characteristics of deep tropical and subtropical convection from nadir-viewing high-altitude airborne doppler radar. *J. Atmos. Sci.*, **67**, 285, doi:10.1175/2009JAS3132.1.

Hong, S. Y., Y. Noh, and J. Dudhia, 2006: A new vertical diffusion package with an explicit treatment of entrainment processes. *Mon. Weather Rev.*, **134**, 2318, doi:10.1175/MWR3199.1.

Houze, R. A., S. G. Geotis, F. D. Marks, and A. K. West, 1981: Winter monsoon convection in the vicinity of North Borneo. Part I: Structure and time variation of the clouds and precipitation. *Mon. Weather Rev.*, **109**, 1595, doi:10.1175/1520-0493(1981)109⟨1595:WMCITV⟩2.0.CO;2.

Hutchins, M. L., R. H. Holzworth, J. B. Brundell, and C. J. Rodger, 2012: Relative detection efficiency of the World Wide Lightning Location Network. *Radio Sci.*, **47**, RS6005, doi:10.1029/2012RS005049.

Iacono, M. J., J. S. Delamere, E. J. Mlawer, M. W. Shephard, S. A. Clough, and W. D. Collins, 2008: Radiative forcing by long-lived greenhouse gases: Calculations with the AER radiative transfer models. *J. Geophys. Res.: Atmos.*, **113**, D13103, doi:10.1029/2008JD009944.

Jacob, D. J., et al., 1997: Evaluation and intercomparison of global atmospheric transport models using ^{222}Rn and other short-lived tracers. *J. Geophys. Res.*, **102**, 5953–5970, doi:10.1029/96JD02955.

Joseph, B., B. C. Bhatt, T. Y. Koh, and S. Chen, 2008: Sea breeze simulation over the Malay Peninsula in an intermonsoon period. *J. Geophys. Res.: Atmos.*, **113**, D20122, doi:10.1029/2008JD010319.

Ju, J. and J. Slingo, 1995: The Asian summer monsoon and ENSO. *Quart. J. Roy. Meteorol. Soc.*, **121**, 1133–1168, doi:10.1002/qj.49712152509.

Kain, J. S. and J. M. Fritsch, 1992: The role of the convective "trigger function" in numerical forecasts of mesoscale convective systems. *Meteor. Atmos. Phys.*, **49**, 93–106, doi:10.1007/BF01025402.

Kanamitsu, M., 1989: Description of the NMC Global Data Assimilation and Forecast System. *Wea. Forecasting*, **4**, 335–342, doi:10.1175/1520-0434(1989)004⟨0335:DOTNGD⟩2.0.CO;2.

Kimura, F. and T. Kuwagata, 1995: Horizontal heat fluxes over complex terrain computed using a simple mixed-layer model and a numerical model. *J. Appl. Meteorol.*, **34**, 549–558, doi:10.1175/1520-0450-34.2.549.

Kistler, R. E. and D. F. Parrish, 1982: Evolution of the NMC Data Assimilation System: September 1978–January 1982. *Mon. Weather Rev.*, **110**, 1335, doi:10.1175/1520-0493(1982)110⟨1335:EOTNDA⟩2.0.CO;2.

Kleist, D. T., D. F. Parrish, J. C. Derber, R. Treadon, W.-S. Wu, and S. Lord, 2009: Introduction of the GSI into the NCEP Global Data Assimilation System. *Wea. Forecasting*, **24**, 1691, doi:10.1175/2009WAF2222201.1.

Klich, C. A. and H. E. Fuelberg, 2013: The role of horizontal model resolution in assessing the transport of CO in a middle latitude cyclone using WRF-Chem. *Atmos. Chem. Phys. Discuss.*, **13**, 14 871–14 925, doi:10.5194/acpd-13-14871-2013.

Krishnamurti, T. N., 1971: Tropical east-west circulations during the northern summer. *J. Atmos. Sci.*, **28**, 1342–1347, doi:10.1175/1520-0469(1971)028⟨1342:TEWCDT⟩2.0.CO;2.

Krishnamurti, T. N. and H. N. Bhalme, 1976: Oscillations of a monsoon system. Part I. Observational aspects. *J. Atmos. Sci.*, **33**, 1937–1954, doi:10.1175/1520-0469(1976)033⟨1937:OOAMSP⟩2.0.CO;2.

Krishnamurti, T. N., M. Kanamitsu, W. J. Koss, and J. D. Lee, 1973: Tropical east-west circulations during the northern winter. *J. Atmos. Sci.*, **30**, 780–787, doi:10.1175/1520-0469(1973)030⟨0780:TECDTN⟩2.0.CO;2.

Lawrence, M. G. and P. J. Crutzen, 1999: Influence of NO_x emissions from ships on tropospheric photochemistry and climate. *Nature*, **402**, 167–170, doi:10.1038/46013.

Leopold, L. B., 1949: The interaction of trade wind and sea breeze, Hawaii. *J. Atmos. Sci.*, **6**, 312–320, doi:10.1175/1520-0469(1949)006⟨0312:TIOTWA⟩2.0.CO;2.

Lepawsky, J., 2005: The Straits of Malacca, gateway or gauntlet? *The Prof. Geographer*, **57 (3)**, 490–492, doi:10.1111/j.0033-0124.2005.493_11.x.

Lin, M., T. Holloway, G. R. Carmichael, and A. M. Fiore, 2010: Quantifying pollution inflow and outflow over East Asia in spring with regional and global models. *Atmos. Chem. Phys.*, **10**, 4221–4239, doi:10.5194/acp-10-4221-2010.

Lin, Y. L., R. D. Farley, and H. D. Orville, 1983: Bulk parameterization of the snow field in a cloud model. *J. Appl. Meteorol.*, **22**, 1065–1092, doi:10.1175/1520-0450(1983)022⟨1065:BPOTSF⟩2.0.CO;2.

Lindzen, R. S. and J. R. Holton, 1968: A theory of the Quasi-Biennial Oscillation. *J. Atmos. Sci.*, **25**, 1095–1107, doi:10.1175/1520-0469(1968)025⟨1095:ATOTQB⟩2.0.CO;2.

Liu, Q., Y. L. Kogan, D. K. Lilly, D. W. Johnson, G. E. Innis, P. A. Durkee, and K. E. Nielsen, 2000: Modeling of ship effluent transport and its sensitivity to boundary layer structure. *J. Atmos. Sci.*, **57**, 2779–2791, doi:10.1175/1520-0469(2000)057⟨2779:MOSETA⟩2.0.CO;2.

Loschnigg, J., G. A. Meehl, P. J. Webster, J. M. Arblaster, and G. P. Compo, 2003: The Asian monsoon, the Tropospheric Biennial Oscillation, and the Indian Ocean zonal mode in the NCAR CSM*. *J. Clim.*, **16**, 1617–1642, doi:10.1175/1520-0442(2003)016⟨1617:TAMTTB⟩2.0.CO;2.

Love, B. S., A. J. Matthews, and G. M. S. Lister, 2011: The diurnal cycle of precipitation over the Maritime Continent in a high-resolution atmospheric model. *Quart. J. Roy. Meteorol. Soc.*, **137**, 934–947, doi:10.1002/qj.809.

Mari, C., D. J. Jacob, and P. Bechtold, 2000: Transport and scavenging of soluble gases in a deep convective cloud. *J. Geophys. Res.*, **105**, 22 255, doi:10.1029/2000JD900211.

Matsumoto, J., 1993: The seasonal changes in asian and australian monsoon regions. *Jpn. Prog. Climatol.*, 39–54.

Matsumoto, J. and T. Murakami, 2000: Annual changes of tropical convective activities as revealed from equatorially symmetric OLR data. *J. of the Meteorol. Soc. of Japan*, **78 (5)**, 543–561.

Matsumoto, J. and T. Murakami, 2002: Seasonal migration of monsoons between the northern and southern hemisphere as revealed from equatorially symmetric and asymmetric OLR data. *J. of the Meteorol. Soc. of Japan*, **80 (3)**, 419–437.

Matthias, V., I. Bewersdorff, A. Aulinger, and M. Quante, 2010: The contribution of ship emissions to air pollution in the north sea regions. *Environ. Pollut.*, **158 (6)**, 2241–2250.

May, P. T. and D. K. Rajopadhyaya, 1999: Vertical velocity characteristics of deep convection over Darwin, Australia. *Mon. Weather Rev.*, **127**, 1056, doi:10.1175/1520-0493(1999)127⟨1056:VVCODC⟩2.0.CO;2.

McGowan, H. and A. Clark, 2008: Identification of dust transport pathways from Lake Eyre, Australia using Hysplit. *Atmos. Environ.*, **42**, 6915–6925, doi:10.1016/j.atmosenv.2008.05.053.

McPherson, R. D., K. H. Bergman, R. E. Kistler, G. E. Rasch, and D. S. Gordon, 1979: The NMC Operational Global Data Assimilation System. *Mon. Weather Rev.*, **107**, 1445, doi:10.1175/1520-0493(1979)107⟨1445:TNOGDA⟩2.0.CO;2.

Meehl, G. A., 1987: The annual cycle and interannual variability in the tropical Pacific and Indian Ocean regions. *Mon. Weather Rev.*, **115**, 27, doi:10.1175/1520-0493(1987)115⟨0027:TACAIV⟩2.0.CO;2.

Meehl, G. A., 1997: The South Asian Monsoon and the Tropospheric Biennial Oscillation. *J. Clim.*, **10**, 1921–1943, doi:10.1175/1520-0442(1997)010⟨1921:TSAMAT⟩2.0.CO;2.

Monin, A. and A. Obukhov, 1954: Basic laws of turbulent mixing in the surface layer of the atmosphere. *Contrib. Geophys. Inst. Acad. Sci. USSR*, **151**, 163–187.

Mori, S., et al., 2004: Diurnal land sea rainfall peak migration over Sumatera Island, Indonesian Maritime Continent, observed by TRMM satellite and intensive rawinsonde soundings. *Mon. Weather Rev.*, **132**, 2021, doi:10.1175/1520-0493(2004)132⟨2021:DLRPMO⟩2.0.CO;2.

Neale, R. and J. Slingo, 2003: The Maritime Continent and its role in the global climate: A GCM study. *J. Clim.*, **16**, 834–848, doi:10.1175/1520-0442(2003)016⟨0834:TMCAIR⟩2.0.CO;2.

Nesbitt, S. W. and E. J. Zipser, 2003: The diurnal cycle of rainfall and convective intensity according to three years of TRMM measurements. *J. Clim.*, **16**, 1456–1475, doi:10.1175/1520-0442-16.10.1456.

Novelli, P. C., K. A. Masarie, and P. M. Lang, 1998: Distributions and recent changes of carbon monoxide in the lower troposphere. *J. Geophys. Res.*, **103**, 19 015, doi:10.1029/98JD01366.

Ohsawa, T., H. Ueda, T. Hayashi, A. Watanabe, and J. Matsumoto, 2001: Diurnal variations of convective activity and rainfall in tropical Asia. *J. of the Meteorol. Soc. of Japan. Ser. II*, **79 (1B)**, 333–352.

Oki, T. and K. Musiake, 1994: Seasonal change of the diurnal cycle of precipitation over Japan and Malaysia. *J. Appl. Meteorol.*, **33**, 1445–1463, doi:10.1175/1520-0450(1994)033⟨1445:SCOTDC⟩2.0.CO;2.

Orville, R. E., 2008: Development of the National Lightning Detection Network. *Bull. Am. Meteorol. Soc.*, **89**, 180, doi:10.1175/BAMS-89-2-180.

Petersen, W. A. and S. A. Rutledge, 2001: Regional variability in tropical convection: Observations from TRMM. *J. Clim.*, **14**, 3566–3586, doi:10.1175/1520-0442(2001)014⟨3566:RVITCO⟩2.0.CO;2.

Pett, R. W. and P. M. Tag, 1984: The sea-breeze-induced coastal calm zone as revealed by satellite data and simulated by a numerical model. *Mon. Weather Rev.*, **112**, 1226, doi:10.1175/1520-0493(1984)112⟨1226:TSBICC⟩2.0.CO;2.

Pielke, R. A., 1974: A three-dimensional numerical model of the sea breezes over South Florida. *Mon. Weather Rev.*, **102**, 115, doi:10.1175/1520-0493(1974)102⟨0115:ATDNMO⟩2.0.CO;2.

Qian, J. H., 2008: Why precipitation is mostly concentrated over islands in the Maritime Continent. *J. Atmos. Sci.*, **65**, 1428, doi:10.1175/2007JAS2422.1.

Ramage, C. S., 1964: Diurnal variation of summer rainfall over Malaysia. *J. Trop. Geog.*, **19**, 62–68.

Ramage, C. S., 1968: Role of a tropical "Maritime Continent" in the atmospheric circulation. *Mon. Weather Rev.*, **96**, 365, doi:10.1175/1520-0493(1968)096⟨0365:ROATMC⟩2.0.CO;2.

Rampanelli, G., D. Zardi, and R. Rotunno, 2004: Mechanisms of up-valley winds. *J. Atmos. Sci.*, **61**, 3097–3111, doi:10.1175/JAS-3354.1.

Rauniyar, S. P. and K. J. E. Walsh, 2011: Scale interaction of the diurnal cycle of rainfall over the Maritime Continent and Australia: Influence of the MJO. *J. Clim.*, **24**, 325–348, doi:10.1175/2010JCLI3673.1.

Richter, A., V. Eyring, J. P. Burrows, H. Bovensmann, A. Lauer, B. Sierk, and P. J. Crutzen, 2004: Satellite measurements of NO_2 from international shipping emissions. *Geophys. Res. Lett.*, **31**, L23110, doi:10.1029/2004GL020822.

Ridley, B., et al., 2004: Florida thunderstorms: A faucet of reactive nitrogen to the upper troposphere. *J. Geophys. Res.: Atmos.*, **109**, D17305, doi:10.1029/2004JD004769.

Rodger, C. J., J. B. Brundell, R. H. Holzworth, and E. H. Lay, 2009: Growing detection efficiency of the World Wide Lightning Location Network. *American Institute of Physics Conference Series*, American Institute of Physics Conference Series, Vol. 1118, 15–20, doi:10.1063/1.3137706.

Rodger, C. J., S. Werner, J. B. Brundell, E. H. Lay, N. R. Thomson, R. H. Holzworth, and R. L. Dowden, 2006: Detection efficiency of the VLF World-Wide Lightning Location Network (WWLLN): initial case study. *Ann. Geophys.*, **24**, 3197–3214, doi:10.5194/angeo-24-3197-2006.

Saji, N. H., B. N. Goswami, P. N. Vinayachandran, and T. Yamagata, 1999: A dipole mode in the tropical Indian Ocean. *Nature*, **401**, 360–363.

Sakurai, N., et al., 2005: Diurnal cycle of cloud system migration over Sumatera Island. *J. of the Meteorol. Soc. of Japan. Ser. II*, **83 (5)**, 835–850.

Salisbury, M., cited 2013: The JOC Top 50 World Container Ports. [Available online at http://www.joc.com/port-news/joc-top-50-world-container-ports_20130815.html].

Sam, N. V., U. C. Mohanty, and A. N. V. Satyanarayana, 2003: Simulation of marine boundary layer characteristics using a 1-D PBL model over the Bay of Bengal during BOBMEX-99. *Indian Acad. of Sci. Proc.: Earth and Planet. Sci.*, **112**, 185–204, doi:10.1007/BF02701986.

Sasaki, T., et al., 2004: Vertical moisture transport above the mixed layer around the mountains in western Sumatra. *Geophys. Res. Lett.*, **31**, L08106, doi:10.1029/2004GL019730.

Satyanarayana, A. N. V., U. C. Mohanty, N. V. Sam, S. Basu, and V. N. Lykossov, 2000: Numerical simulation of the marine boundary layer characteristics over the Bay of Bengal as revealed by BOBMEX-98 Pilot experiment. *Indian Acad. of Sci. Proc.: Earth and Planet. Sci.*, **109**, 293–303, doi:10.1007/BF02702203.

Schumacher, C. and R. A. Houze, Jr., 2003: Stratiform rain in the tropics as seen by the TRMM Precipitation Radar*. *J. Clim.*, **16**, 1739–1756, doi:10.1175/1520-0442(2003)016⟨1739:SRITTA⟩2.0.CO;2.

Skamarock, W. C., et al., 2008: A description of the advanced research WRF version 3. *NCAR technical note NCAR/TN/u2013475+ STR*.

Streets, D. G., G. R. Carmichael, and R. L. Arndt, 1997: Sulfur dioxide emissions and sulfur deposition from international shipping in Asian waters. *Atmos. Environ.*, **31**, 1573–1582, doi:10.1016/S1352-2310(96)00204-X.

Streets, D. G., S. K. Guttikunda, and G. R. Carmichael, 2000: The growing contribution of sulfur emissions from ships in Asian waters, 1988-1995. *Atmos. Environ.*, **34**, 4425–4439, doi:10.1016/S1352-2310(00)00175-8.

Tewari, M., et al., 2004: Implementation and verification of the unified Noah land surface model in the WRF model (Formerly Paper Number 17.5). *20th Conference on Weather Analysis and Forecasting/16th Conference on Numerical Weather Prediction*.

U.S. DOT, cited 2013: Top 25 Flags of Registry. [Available online at http://www.marad.dot.gov/library_landing_page/data_and_statistics/Data_and_Statistics.htm].

Virts, K. S., J. A. Thornton, J. M. Wallace, M. L. Hutchins, R. H. Holzworth, and A. R. Jacobson, 2011: Daily and intraseasonal relationships between lightning and NO_2 over the Maritime Continent. *Geophys. Res. Lett.*, **38**, L19803, doi:10.1029/2011GL048578.

Virts, K. S., J. M. Wallace, M. L. Hutchins, and R. H. Holzworth, 2013: Diurnal lightning variability over the Maritime Continent: Impact of low-level winds, cloudiness, and the MJO. *J. Atmos. Sci.*, **70**, 3128–3146, doi:10.1175/JAS-D-13-021.1.

von Glasow, R., M. G. Lawrence, R. Sander, and P. J. Crutzen, 2003: Modeling the chemical effects of ship exhaust in the cloud-free marine boundary layer. *Atmos. Chem. Phys.*, **3**, 233–250.

Waliser, D. E. and C. Gautier, 1993: A Satellite-derived climatology of the ITCZ. *J. Clim.*, **6**, 2162–2174, doi:10.1175/1520-0442(1993)006⟨2162:ASDCOT⟩2.0.CO;2.

Wang, B., 1994: Climatic regimes of tropical convection and rainfall. *J. Clim.*, **7**, 1109–1130, doi:10.1175/1520-0442(1994)007⟨1109:CROTCA⟩2.0.CO;2.

Wang, C. and R. G. Prinn, 2000: On the roles of deep convective clouds in tropospheric chemistry. *J. Geophys. Res.*, **105**, 22 269, doi:10.1029/2000JD900263.

Wang, F., D. S. Chen, S. Y. Cheng, L. J. B., L. M. J., and R. Z. H., 2010: Identification of regional atmospheric PM_{10} transport pathways using HYSPLIT, MM5-CMAQ and synoptic pressure pattern analysis. *Environ. Model. & Softw.*, **25 (8)**, 927 – 934, doi: http://dx.doi.org/10.1016/j.envsoft.2010.02.004.

Weisman, M. L., W. C. Skamarock, and J. B. Klemp, 1997: The resolution dependence of explicitly modeled convective systems. *Mon. Weather Rev.*, **125**, 527, doi:10.1175/1520-0493(1997)125⟨0527:TRDOEM⟩2.0.CO;2.

Williams, E. J., B. M. Lerner, P. C. Murphy, S. C. Herndon, and M. S. Zahniser, 2009: Emissions of NO_x, SO_2, CO, and HCHO from commercial marine shipping during Texas Air Quality Study (TexAQS) 2006. *J. Geophys. Res.: Atmos.*, **114**, D21306, doi:10.1029/2009JD012094.

Wissmeier, U. and R. Goler, 2009: A comparison of tropical and midlatitude thunderstorm evolution in response to wind shear. *J. Atmos. Sci.*, **66**, 2385, doi:10.1175/2009JAS2963.1.

Wu, C. H. and H. H. Hsu, 2009: Topographic influence on the MJO in the Maritime Continent. *J. Clim.*, **22**, 5433, doi:10.1175/2009JCLI2825.1.

Wu, P., J. I. Hamada, S. Mori, Y. I. Tauhid, M. D. Yamanaka, and F. Kimura, 2003: Diurnal variation of precipitable water over a mountainous area of Sumatra Island. *J. Appl. Meteorol.*, **42**, 1107–1115, doi:10.1175/1520-0450(2003)042⟨1107:DVOPWO⟩2.0.CO;2.

Yang, G. Y. and J. Slingo, 2001: The diurnal cycle in the tropics. *Mon. Weather Rev.*, **129**, 784, doi:10.1175/1520-0493(2001)129⟨0784:TDCITT⟩2.0.CO;2.

BIOGRAPHICAL SKETCH

Tristan Hall was raised in the one-horse town of Genoa, Ohio. His parents are Pattie and David Hall. He is the youngest of three brothers who are all very close.

In elementary school, his advisor asked him what he wanted to be when he grew up. He answered simply "doctor," as many children do, and "storm chaser." After high school Tristan followed his brothers to Appalachian State University. During his time at ASU, he met and fell hopelessly in love with a brilliant violinist named Catherine Williams. As he progressed in his studies, Tristan became increasingly interested in meteorology. One of his professors would give a daily weather synopsis that sparked more and more interest in meteorology from Tristan. Unfortunately, Appalachian State does not have a meteorology degree program. Instead, Tristan decided to double major in physics and geography with concentrations in the atmosphere. Additionally, he earned a minor in mathematics to supplement his work in the sciences. When it was time to apply for graduate school, Tristan had only one institution in mind: Florida State University. He applied only to Florida State and was accepted in 2010.

While studying at Florida State, Tristan participated in a DOE project called MC3, and was stationed in Vici, Oklahoma for a month during May 2011. His job was to release weather balloons that measured atmospheric conditions during convectively active days (some of which produced numerous tornadoes). While he was in Vici, he got the chance to storm chase. He witnessed a rope tornado that was an EF-3 at its strongest stage.

Tristan joined Dr. Henry E. Fuelberg's lab in his third semester at Florida State. As part of this lab, Tristan was able to participate in a NASA field campaign called SEAC^{4}RS in the summer of 2013. This campaign allowed Tristan to get first-hand, real-world experience operationally forecasting for science flights. Each mission cost hundreds of thousands of dollars, and mistakes were not allowed. He had the opportunity to present and argue his forecast in front of influential NASA employees and highly-respected meteorologists. Before and during SEAC^{4}RS, Tristan also managed a group of graduate students for another NASA campaign called SEACIONS. The group released ozonesondes that measured atmospheric ozone concentrations.

After completing his master's degree, Tristan will continue his work at Florida State in the PhD meteorology program, with a focus on tropical cyclone rainfall prediction.